PHANEROZOIC SEDIMENTARY COVER HISTORY OF THE HUDSON PLATFORM: A HEURISTIC MODELING PERSPECTIVE

non-peer reviewed manuscript preprint submitted to:

American Journal of Science

KALIN T. McDANNELL[*,†], PAUL B. O'SULLIVAN[**], KERRY GALLAGHER[***], and SCOTT BOROUGHS[§]

[*]Department of Earth Sciences, Dartmouth College, Hanover, NH 03775, United States
[**]GeoSep Services, 1521 Pine Cone Road, Moscow ID 83843, United States
[***]Géosciences Rennes, Université de Rennes 1, Rennes 35042, France
[§]School of the Environment, Washington State University, Pullman WA 99164, United States

preprint doi: https://www.doi.org/10.31223/X5M05W
compiled November 9, 2022

ABSTRACT. Understanding the long-term erosion and burial history of cratons is challenging due to the incompleteness of the rock record. Low-temperature thermochronology is used to elucidate these surface histories by inverting thermochronological data for the time-temperature history and incorporating sparse constraints and other assumptions about the regional geologic evolution. However, imposing certain assumptions will influence the form of the inferred thermal histories, and in some cases this step may limit impartial assessment of the unknown history in terms of what features are required by the data and those that the data are consistent with (or at least do not contradict). Here we present a study involving laser ablation apatite fission-track data from three central Canadian Shield basement samples collected adjacent to the Hudson Platform Ordovician nonconformity in northern Manitoba and Ontario. Compared to a conventional fission-track analysis, our samples are characterized by up to ~3× the number of dated age grains and > 6–8× the number of track length measurements. The additional data improve inferences that are conditional on the data in Bayesian QTQt inversions, which in turn provide guidance on the potential conditions necessary for informing classical Frequentist inversions using the AFTINV software. Thermal history modeling is thus guided by a heuristic philosophy regarding the use of explicit constraints, which allows us to (i) examine the ability of the Bayesian model to independently infer geologically plausible time-temperature paths from the data (that is, assess sensitivity), (ii) compare the results with the known geology, and (iii) recursively parameterize models with respect to the previous results. QTQt models without time-temperature constraint boxes suggest two reheating events better explain the fission-track data (compared to a monotonic-cooling scenario) and indirectly imply periods at cooler, near-surface conditions in the latest Neoproterozoic to early Paleozoic, and in the Jurassic to early Cretaceous. The timing of such periods are consistent with major Hudson Platform unconformities. Collectively, best-fitting inverse thermal histories establish that the presently exposed basement near the Hudson Bay Basin experienced peak Paleozoic burial at *ca.* 317 ± 36 Ma (2σ). Burial could have occurred as early as Famennian or as late as Carnian time. A second burial event occurred in the latest Mesozoic to Tertiary at *ca.* 46 ± 30 Ma, but could have been as early as Aptian and as late as Chattian time. The sample furthest to the east nearer to the Moose River Basin may have experienced peak burial conditions earlier at 83 ± 14 Ma (within uncertainty of other models), synchronous with late Cretaceous sea-level rise. These estimates are in broad agreement with the preserved regional geology and previous thermochronology studies. However, our models support peak burial during Pennsylvanian and Eocene times, which could suggest a more extensive sedimentary cover than implied from preserved Hudson Bay Basin rocks (of well-known depositional age). Such histories are broadly consistent with Williston Basin and Slave craton burial history reconstructions to the west. Sedimentary rocks are estimated to have been ~1.4 ± 0.7 km (2σ) thick in the Paleozoic and ~1.5 ± 0.9 km thick in the latest Mesozoic to middle Cenozoic.

Key words: apatite fission track · Canadian Shield · thermochronology · burial history · Hudson Platform

†Corresponding Author: kalin.t.mcdannell@dartmouth.edu

INTRODUCTION

Fission-Track Thermochronology and Continental Surface Histories

Cratons are the ancient nuclei of continents that have remained tectonically stable since the Archean–Paleoproterozoic. These shield regions are typically characterized by low topographic relief and Precambrian igneous and metamorphic basement exposed at the surface. Many cratons are devoid of sedimentary cover—making reconstruction of their post-orogenic geological history difficult since we often only have brief 'snapshots' of past geological events or processes in the rock record. For example, most of the Canadian interior is comprised of Precambrian basement sporadically covered only by thin early-middle Paleozoic or middle-late Mesozoic sedimentary strata (Sloss, 1963; Norris & Sanford, 1968; Norris, 1977; Telford & Long, 1986; Sanford, 1987; Norris, 1993; Pinet and others, 2013; Burgess, 2019; Lavoie and others, 2019)—leaving the details about the Phanerozoic geological history an open question. Apatite fission-track (AFT) dating has long been one of the primary thermochronological tools used to reconstruct this missing record and constrain the potentially complex burial and erosion history of the North American craton (Crowley and others, 1986; Crowley & Kuhlman, 1988; Naeser & Crowley, 1990; Crowley, 1991; Kohn and others, 1995, 2002; Osadetz and others, 2002; Lorencak and others, 2004; Kohn and others, 2005; Feinstein and others, 2009; Pinet and others, 2016; McDannell and others, 2019b; Pinet & McDannell, 2020). More recently, (U–Th)/He thermochronology has been successfully applied to understand cratonic evolution worldwide (for example, Flowers and others, 2006; Ault and others, 2009; Guenthner and others, 2017; Baughman & Flowers, 2020; Morón and others, 2020), but we focus on application of the AFT method in this contribution.

The fission-track thermochronometer provides time and temperature information from the damage features or tracks produced by the energetic fission of ^{238}U within the mineral crystal lattice (Fleischer and others, 1965). The number of spontaneous tracks per unit area is related to the amount of U in the apatite and thus can provide an estimate of the time (that is, apparent age) over which tracks have accumulated in the crystal. Fission tracks form continuously over time with an initial etched length of ~16–17 μm, and fade or anneal when subjected to higher temperature, resulting in a nearly equivalent reduction in track density (per area) across an etched grain surface (Gleadow & Duddy, 1981). Early observations of borehole samples showed that with increasing depth, mean track length is reduced (that is, annealed) with increasing temperature (Gleadow and others, 1986b; fig. 1). As a consequence, annealing decreases the apparent age of the sample as each track is shortened to a degree reflecting the maximum temperature experienced during its history before being totally annealed at approximately 100–120°C (Gleadow & Duddy, 1981; Green and others, 1986; Gleadow and others, 1986a). Laboratory experiments have also demonstrated that resistance to thermal annealing is influenced by apatite composition, primarily Cl and various elemental substitutions that enhance track retentivity compared to common fluorapatite, such as: Fe, Mg, Mn, Na, OH, Si, and Sr (Green and others, 1985; Carlson, 1990; Crowley and others, 1990; Carlson and others, 1999; Barbarand and others, 2003; Ravenhurst and others, 2003; Tello and others, 2006). Apatite composition is measured directly by electron microprobe or laser ablation inductively coupled plasma mass spectrometry

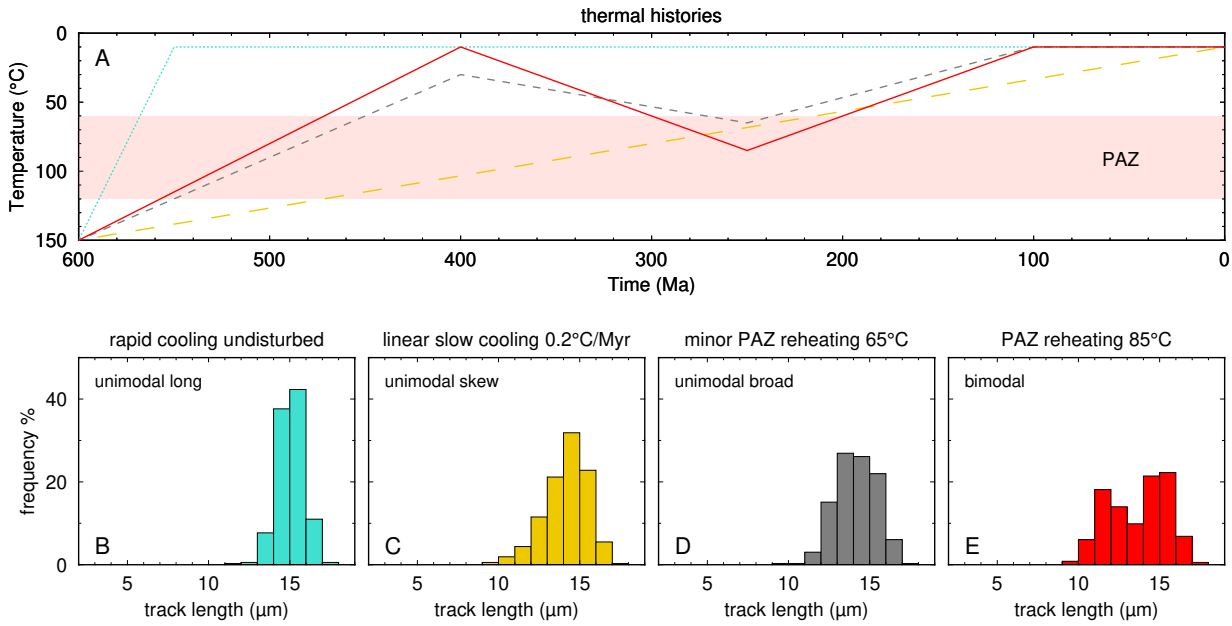

Fig. 1. A) Hypothetical thermal history scenarios and the corresponding *c*-axis projected track length distributions produced from each t–T path. Rapid cooling (blue dotted line), slow cooling (yellow long dash line), minor PAZ reheating (gray short dash line), and greater PAZ reheating (red solid line). B) unimodal long track lengths corresponding to rapid cooling and subsequent stasis. C) unimodal right skew track length distribution typical of simple, slow cooling. D) unimodal track length distribution that has been shortened and broadened due to reheating to 65°C. E) bimodal track length distribution due to a history involving greater reheating to 85°C.

(LA-ICPMS)—although it is commonly estimated indirectly by proxy with the D_{par} parameter (track etch-pit diameter; Donelick and others, 2005). Apatite chemistry is used to approximate track annealing kinetics, which are a critical requirement for thermal history modelling (Laslett and others, 1987; Ketcham and others, 1999; Donelick and others, 2005; Ketcham and others, 2007; Ketcham, 2019).

The temperature range of the AFT partial annealing zone (PAZ; ~120–60°C) varies as a function of the annealing kinetics and the rock cooling rate (Gleadow & Duddy, 1981; Green and others, 1986; Gleadow and others, 1986a; Duddy and others, 1988). Fission-track apparent ages can broadly inform us about the overall duration of, and sometimes timing of events in the overall thermal history. The length of a given fission track will reflect to a large degree the maximum temperature that track experienced, whereas a distribution of track lengths provides key information on the structure of the thermal history (for example, Gleadow and others, 1986a,b). Thus models of how fission tracks anneal are essential for the accurate modelling and interpretation of track length data (Ketcham and others, 1999, 2007; Ketcham, 2019) and provide additional information about thermal history style that is unavailable to most other thermochronometers. Figure 1 conceptually demonstrates this for four different simplified thermal histories using a forward model, including: (1) rapid cooling followed by isothermal conditions at the Earth's surface; (2) linear, slow cooling at a typical cratonic rate of ~0.2°C/My; (3) slow cooling to the surface, followed by reheating to 65°C and cooling out of the PAZ; and (4) same style as history 3 except reheating to 85°C within the PAZ. Each of these histories produce characteristic track length distributions (fig. 1B–E) that are diagnostic of the

type of history the AFT sample experienced. The histories in fig. 1A yield either, a unimodal (normal) distribution of long track lengths of ~15 μm for the rapid cooling scenario; a unimodal negative skew distribution for slow cooling with a mean length of ~14 μm; a unimodal broad or flattened distribution with a similar mean length as the slow cooling case; and a bimodal distribution for the 85°C reheating example. The progression from fig. 1B–E generally shows that track length distributions become broader and shorter with increased magnitude and duration of heating. From these simple demonstration, we can see that track lengths are critical for understanding the thermal history of a rock.

MOTIVATIONS

Inverse Modelling Philosophies: Evidence of Absence or Absence of Evidence

We are interested in exploiting the information contained in thermochronological data to determine the long-term surface history of the Hudson Platform (North American craton) by utilizing the limited sedimentary record to inform and validate thermal history models. We also show that different modelling strategies can be used to support and cross-validate interpretations. First we discuss conventional approaches to data collection and thermochronological inverse modelling and then elaborate on some of the specific modelling considerations for deep-time problems. In most cratonic studies, many samples are often collected across a broad region and rocks then undergo standard thermochronological analysis. Here we focus only on AFT dating. AFT data are modelled utilizing a supporting framework of geological constraints for a given study area. More often than not these "constraints" are a mix of physical geology, assumptions, and geologic interpretations—which are not equal in terms of reliability and entail different degrees of uncertainty (McDannell and others, 2022b). The lack of physical geologic constraints to inform modelling is problematic for basement terranes when trying to reconstruct the time-temperature (t–T) histories from these data (McDannell & Flowers, 2020; Green & Duddy, 2021; McDannell & Issler, 2021). This dilemma is commonly addressed by utilizing whatever geologic information we have, however, unless samples are taken directly from well-constrained locations (for example, near unconformities; McDannell & Keller, 2022), there is typically some degree of regional extrapolation of, or uncertainty in, assumptions about past conditions. In some situations these regional inferences may be warranted, whereas in others they may not, and it is difficult to know which is the case before carrying out modelling. The presumed validity of such assumptions is also called into question due to the decrease in chronometer resolution and increase in thermal history non-uniqueness with time (McDannell & Flowers, 2020).

Many published t–T inversions are posed as "hypothesis tests" to determine if the chronometer data can be explained by, or are consistent with, a specific geologic scenario. While this approach is valid, if the data are not sensitive to a certain imposed constraint then a hypothesis is not being tested (for example, a chronometer is thermally reset in the Phanerozoic but a near-surface constraint is applied in the Proterozoic). Depending on the type of inversion methodology, this sort of model can be misleading and provide false confidence in a particular

scenario. The correlation of model parameters (that is, time and temperature; see Willett, 1997; Fox & Carter, 2020), the uncertainties related to kinetic (annealing) models, and the precision of the AFT data can inhibit clear delineation between features of histories that are required by the data versus those that are allowed in a specific geological context. Put another way, the ability to obtain t–T solutions that adequately fit thermochronologic data with the use of t–T boxes in a model does not prove that such constraints are "correct" or required by the data—it merely demonstrates the data do not (or cannot) contradict the imposed constraints (Gallagher, 2016, 2021).

While indisputable geologic information should be incorporated into inverse models if available, it is often unavailable in sufficient detail in many settings. Therefore, of equal concern are studies that incorporate few thermochronometric data and attempt to discern geological histories over hundreds of millions of years—without adequate time-temperature resolution (or independent data) this will nearly always result in simple, monotonic cooling histories (see Discussion). One of the criticisms of Bayesian t–T modelling is that "slow continuous cooling is a common assumption" for basement terranes (for example, Green and others, 2020; Green & Duddy, 2021). This is likely due to the perception that Bayesian modelling strictly adheres to a philosophy akin to Occam's Razor—where the simplest answer is preferred. This sort of answer is often obtained when low resolution data are modelled without additional geological context, since for example, it is relatively easy to reproduce a single thermochronometric datum with a linear history. It does not mean, however, that a simple history is implicitly assumed or that one will *always* be recovered. This is contrasted with a random Monte Carlo (Frequentist) t–T modelling approach (for example, Issler, 1996; Ketcham, 2005; Murray and others, 2022) that explicitly requires the incorporation of external information to produce results. A critical point is that thermal history simulations are conditional on the imposed constraints and the assumptions/limitations of kinetic models, regardless of the statistical model framework.

An outstanding problem relates then to our ability to resolve more complex thermal histories in the absence of firm geological constraints. For instance, the Hudson Platform of central Canada (Sanford & Norris, 1973) is a large area of Precambrian basement lacking contiguous Phanerozoic strata—eliciting the question: were the currently exposed basement rocks buried in the past? If they were not—does this vary spatially? If they were—then when were they buried and by how much? The reflexive (and more interesting) assumption would be that the basement *was* buried by sedimentary cover and to simply fix the timing of regional unconformities within inversions—but this can become circular if our model simply confirms our preferred hypothesis without testing other possibilities (McDannell and others, 2022b). An alternative approach is to first minimize prior assumptions about a thermal history and to examine the sensitivity and resolving power of the data (for example, Fox & Carter, 2020; Gallagher, 2021; McDannell & Issler, 2021; McDannell and others, 2022a,b).

Simulations in this paper were performed in the Bayesian QTQt software (Gallagher, 2012) to illustrate what can be resolved (or not) by implementing a recursive and heuristic modelling approach. We first minimized the use of constraints as time-temperature "boxes" that force the model to take an predefined path in certain part of the history, allowing us to instead examine the ability of the model to independently infer geologically plausible

t–T paths from the thermochronological data (and Bayesian general prior assumptions). This was followed by examining the "unconstrained" models and determining regions of t–T space that were well resolved and those parts that did or did not agree with the known geology. That information was then explicitly applied as constraints in another set of inversions (to be clear, the 'unconstrained' models establish the baseline t–T sensitivity of the data and are not necessarily interpreted as a preferred thermal history). The QTQt models were also compared to results generated using the AFTINV software (Issler, 1996; Issler and others, 2022). The AFTINV models are informed by the QTQt results, yet are constructed with the more prevalent 'hypothesis test' modelling philosophy in mind (that is, continuous cooling vs. one peak vs. two-peak history), which is inherent to software employing Frequentist statistics. AFTINV (and other software like it) naturally require more explicit boundary conditions and user-specified constraints to reproduce the observed data and achieve model convergence. The methods and results discussed here offer a progressive approach that explores some of the ways inverse modelling can not only inform but assist in deciphering the complex surface history of cratons.

"Far better an approximate answer to the right question, which is often vague, than an exact answer to the wrong question, which can always be made precise." (Tukey, 1962)

CASE STUDY: HUDSON PLATFORM, CANADIAN SHIELD

Brief Geologic Overview

The pervasive view is that the Canadian Shield has experienced long-term quiescence over hundreds of millions to billions of years, with the canonical null hypothesis being that the majority of exposed basement has persisted in its current geomorphological state throughout the Phanerozoic—subaerially exposed and unburdened by thick sedimentary cover. However, this view may be incomplete since the shield may have only recently been altogether denuded during Laurentide glaciation (for example, Sugden, 1978; Bell & Laine, 1985; Licciardi and others, 1998). Other indirect evidence suggests that craton surface evolution was much more dynamic. Many studies infer periodic burial during high sea-level excursions (for example, Bond, 1978; White and others, 2000) and erosion during epeirogenic mantle (thermal) perturbations (for example, Ahern & Mrkvicka, 1984; Crowley & Kuhlman, 1988; Burgess and others, 1997; Flowers and others, 2012) or Precambrian continental glaciations (for example, White, 1973; McDannell and others, 2022a; McDannell & Keller, 2022). Of course, tectonic processes such as plate reorganization(s) and peripheral orogenesis (for example, Sanford and others, 1985; Crowley, 1991; Kohn and others, 2005; Ault and others, 2009; Feinstein and others, 2009) may have contributed to both cratonic burial and erosion. To better understand continental interior surface evolution, three crystalline basement samples were collected from central Canada that have reliable, yet limited geologic information (described below) to support thermal history modelling.

Geologic Context for Fission-Track Samples

The Hearne Domain lies in the Churchill Province of the shield (Fig. 2) and is comprised of Neoarchean granitoids, greenstones, metasedimentary and volcanic rocks, and Paleoproterozoic granites that flank reworked late Paleoproterozoic basement to the south (Fig. 2; Hoffman, 1988, 1989; Weller & St-Onge, 2017), and the Paleozoic–Mesozoic Hudson Bay sedimentary basin to the east (Pinet and others, 2013). The Superior Province is the nucleus of the Canadian Shield and contains an assemblage of some of the oldest rocks on Earth, including Archean oceanic and continental terranes that collided and underwent Neoarchean metamorphism and cratonization by *ca.* 2700–2600 Ma (Percival and others, 2012). The central Canadian Shield is generally considered to have been tectonically stable since intracratonic basin formation at *ca.* 1700 Ma (Fraser and others, 1970; Rainbird and others, 2007) following the Tran-Hudson Orogeny (THO; for example, Schneider and others, 2007) and the assembly of Laurentia at *ca.* 1800 Ma (Hoffman, 1988, 1989).

Regional geologic context for the Phanerozoic, with respect to the sample locations is as follows. The Hearne Domain sample (97-10-365) is from exposed granodiorite basement within the Seal River Fold Belt (Anderson and others, 2010; Rayner, 2010). This location is at the erosional edge of the Hudson Bay Paleozoic nonconformity at the mouth of the Seal River in northeastern Manitoba (fig. 2). The THO sample (CB99-227) was collected from a foliated biotite tonalite from Stephens Lake, ~28 km from the Paleozoic unconformity in Manitoba. Sample 12RM086 was collected from a porphyritic K-feldspar quartz monzonite in the western Superior Province "Ring of Fire" region in northern Ontario (fig. 2), ~50 km west of the present-day erosional edge of the Paleozoic unconformity in the area of McFaulds Lake (Metsaranta & Houlé, 2017). Preliminary fission-track data for this sample were first reported in McDannell and others (in press).

The Hudson Bay Basin is a large intracratonic sag basin that has preserved section of over 2500 m (fig. 2 and fig. 3), primarily consisting of Upper Ordovician to Upper Devonian shallow marine rocks overlain by inferred Cretaceous strata (Norris & Sanford, 1968; Pinet and others, 2013; Lavoie and others, 2015). The Ordovician rocks in the Hudson Bay region are Edenian to Richmondian in age (*ca.* 454–444 Ma; Nelson, 1963; Armstrong and others, 2018; Zhang & Riva, 2018), but are as old as *ca.* 475 Ma in the northerly Foxe Basin (Trettin, 1975). The onshore basal Paleozoic section of the Hudson Bay Basin is the middle Upper Ordovician Portage Chute Formation of the Bad Cache Rapids Group (Lavoie and others, 2019, for summary), which is *ca.* 453–447.5 Ma in age (Maysvillian Stage) or *ca.* 470–450 Ma in age, depending on the location and applied age model (Peters and others, 2018; Gradstein and others, 2020). Refer to McDannell & Keller (2022) and McDannell and others (in press) for further discussion.

Much of the later Phanerozoic sedimentary record is highly fragmented or absent. Tillement and others (1976) first reported the presence of marine Pennsylvanian rocks from pollen assemblage analysis of samples from the Narwhal O-58 well in Hudson Bay. Those findings were disputed as additional biostratigraphic work found mixed Westphalian (*ca.* 315–306 or ICS stages Bashkirian–Kasimovian), Cretaceous, and Tertiary microfossils (Williams & Barrs, 1976). The earlier results and interpretations of Tillement and others (1976) were instead attributed to

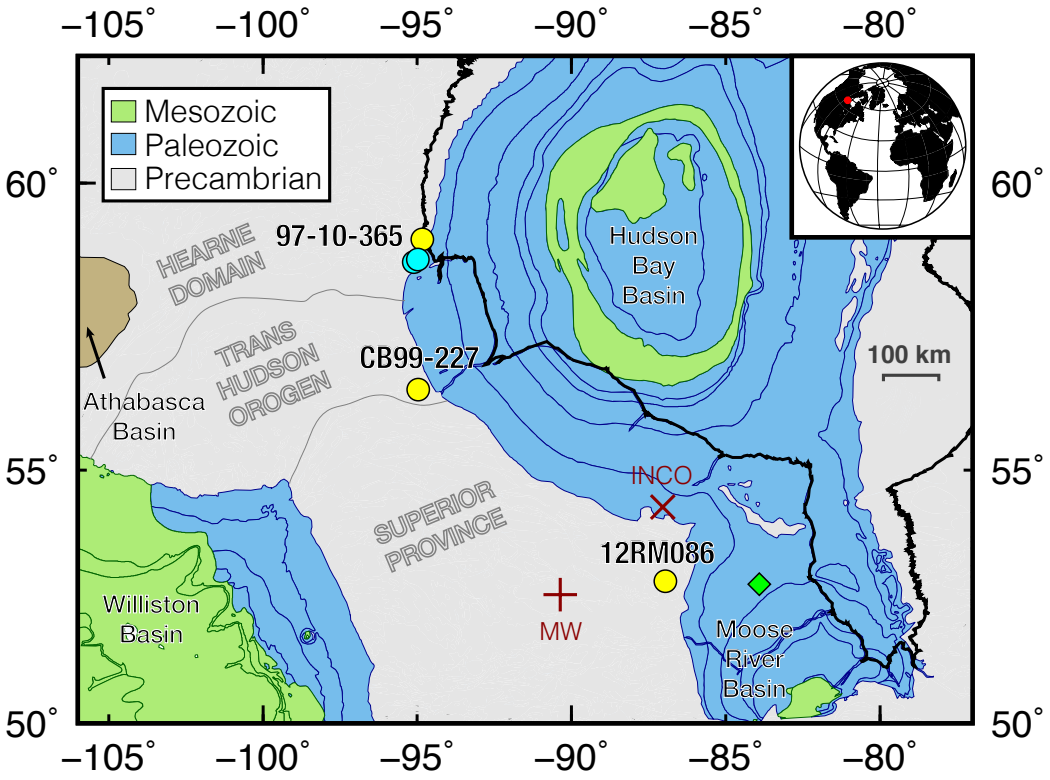

Fig. 2. Simplified geologic map of the central Canadian Shield near Hudson Bay, modified from Wheeler and others (1996). New AFT sample locations are yellow points across the Hudson Platform. Light blue points (near sample 97-10-365) are multi-chronometer samples published in McDannell & Keller (2022). Precambrian rocks are undifferentiated except for those rocks of the *ca.* 2.0–1.8 Ga Trans-Hudson Orogen (THO). The *ca.* 1.7 Ga Athabasca Basin lies to the west of Hudson Bay. The Hudson Bay Basin Paleozoic section outcrops (blue) along the THO and the western Superior Province. Green diamond is the approximate location of the *ca.* 170 Ma Attawapiskat kimberlite field. MW denotes the location of the Musselwhite gold mine, those AFT data discussed in Pinet & McDannell (2020). INCO is the borehole discussed in Galloway and others (2012); refer to the text for discussion. Inset map provides global reference.

"drilling contamination" by Williams & Barrs (1976) but those conclusions remain controversial. The adjacent Moose River Basin (fig. 2) contains Upper Ordovician through Upper Devonian strata with a major unconformity overlain by erosional remnants of minor Middle Jurassic (Bajocian–Bathonian, 170–165 Ma; Norris, 1977) and unconformable Early Cretaceous (Albian and Aptian; *ca.* 121–100 Ma) rocks (Norris & Sanford, 1968; Norris, 1977; Telford & Long, 1986). The *ca.* 180–170 Ma hypabyssal facies kimberlites in the Attawapiskat vicinity of the Moose River Basin (Fig. 2) were erupted subaerially through basement and thin Paleozoic cover (Kong and others, 1999; Sage, 2000; Webb and others, 2004). The INCO-Winisk #49204 borehole (fig. 2) also contains palynological evidence of Aptian–Turonian (*ca.* 120–90 Ma) sediment recycling and sediments preserved at ~70 m depth of Miocene age unconformably overlying the Paleozoic section (Galloway and others, 2012). The regional applicability of this constraint is uncertain but there are isolated occurrences of thin Tertiary strata along the southern Hudson Bay Basin in northern Ontario and Manitoba (Lavoie and others, 2013).

The Williston Basin lies to the southwest of our samples (fig. 2) and contains thick basin fill of > 4 km deposited during the Phanerozoic (Burrus and others, 1996), beginning with the platform onlap of the Sauk sequence (Sloss,

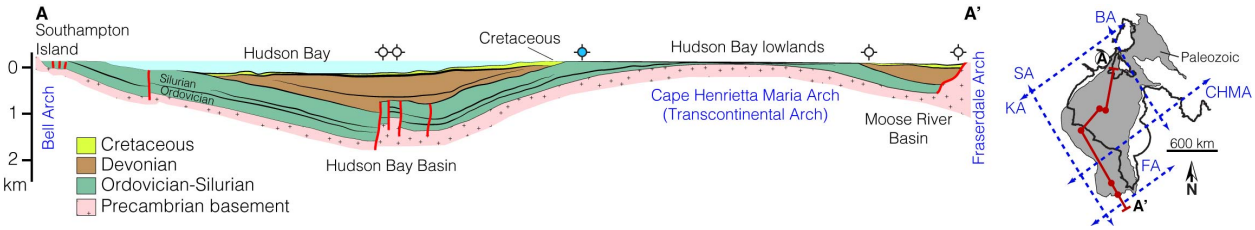

Fig. 3. Geological cross-section across Hudson Bay Basin, modified from Norris (1993) and McDannell and others (in press). The Phanerozoic geology is simplified and grouped according to sequences in Sloss (1963). Red lines are intra-basin faults. Gray area in the inset outlines Paleozoic and younger rocks (refer to Pinet and others, 2013) and major regional arch structures are shown as dashed blue lines (for example, Sanford & Grant, 1990): Bell arch (BA); Cape Henrietta Maria arch or Transcontinental arch (CHMA); Fraserdale arch (FA); Keewatin arch (KA); Severn arch (SA; trending NW-SE). The dark red line A–A' in the cross-section extends from Southampton Island to the Moose River Basin and the points along the line correspond to drilled hydrocarbon exploration wells in the Hudson Bay Basin. The Comeault #1 well in Manitoba is the closest to our northerly samples that penetrated over 550 m of Silurian through Ordovician rocks and Precambrian basement at 616 m depth (third point from the bottom in the inset and the blue dot on the cross-section; Armstrong and others, 2018; Lavoie and others, 2019).

1963; Norris & Sanford, 1968; Sanford, 1987). The basin was undergoing rapid subsidence after *ca.* 488 Ma (or earlier) during deposition of the Deadwood Formation and the Middle Ordovician Winnipeg Formation (ca. 471–458 Ma depositional age; LeFever, 1996). A major angular unconformity exists in the basin between Mississippian and Triassic strata (*ca.* 325–220 Ma; Butcher and others, 2012) implying possible near-surface conditions for Precambrian basement across the shield during that interval. Regionally, an episode of Paleozoic heating ranging between ~70–100 °C has been documented for Precambrian basement located to the southwest and east of the Hudson Bay Basin—attributed to geodynamics related to intracratonic basin formation (Crowley & Kuhlman, 1988; Crowley, 1991; Osadetz and others, 2002) and the distal effects of Appalachian orogenesis, respectively (Lorencak and others, 2004; Kohn and others, 2005; Feinstein and others, 2009). This contrasts with thermal history modelling results for AFT samples from the Musselwhite gold mine in northern Ontario that indicate Paleozoic–Mesozoic heating was limited or absent (Pinet & McDannell, 2020). These spatial differences may be due to the subtle effects of paleo-arch systems across the southern shield (Sanford and others, 1985; Sanford, 1987; Sanford & Grant, 1990). These basement-controlled, physiographic elements, such as the well-known Transcontinental arch (fig. 3), were positive topographic features that conceivably influenced regional sediment dispersal and depositional patterns during the latest Precambrian (?) through the mid-Paleozoic (Sanford and others, 1985; Sanford & Grant, 1990). Published AFT patterns of older ages and longer track lengths near the Severn arch (oriented NW–SE near the Musselwhite mine) and Trancontinental arch in the western Superior Province (Kohn and others, 2005) at the very least indicate areas that were not deeply buried, but also potentially denote the presence of early Phanerozoic topographic highs.

To summarize, regional information suggests that Precambrian basement was exhumed prior to or by *ca.* 460 Ma. Of critical importance is the fact that basement may have been subaerial for 50–100 Myr (or more?) prior to the Ordovician unconformity. Burial of the shield occurred primarily during the Ordovician through Devonian (Patchett and others, 1999). Subaerial basement exposure may have occurred during the Mississippian through the Jurassic,

followed by deposition during the Cretaceous or early Tertiary, with final exhumation beginning by the early Tertiary or after approximately Oligocene–Miocene time. We present new AFT analytical results, which are modelled to assess whether our data can yield thermal histories that are independently consistent with the accepted regional geological evolution. There is also the question of whether the currently exposed Hudson Platform basement was buried during deposition of the Hudson Bay sequence. Burial of basement in the early Paleozoic is likely for our samples due to their close proximity to the Ordovician nonconformity.

METHODS AND RESULTS

LA-ICPMS Fission Track and U-Pb Apatite Double Dating

Apatite grains were double-dated by LA-ICPMS (Chew & Donelick, 2012) using the modified ζ-calibration method for fission track dating (Cogné and others, 2020), with the Durango and McClure Mountain (MMhb) age standards for LAFT and U-Pb data acquisition, respectively. The AFT pooled age obtained in analytical sessions for Durango was 31.4 ± 1.6 Ma (2σ) and 256 ± 14 Ma for McClure Mountain apatite. The weighted mean U-Pb age of McClure Mountain apatite was 525 ± 27 Ma (2σ). All ages are in agreement with accepted previously published values (see Chew & Donelick, 2012). All analytical methods are the same as those discussed in McDannell and others (2019a) and McDannell and others (2019b). Single laser-ablation spots were chosen within minimized grain counting areas to avoid potential U zonation and all analytical results are shown in table 1, table 2, and table 3 (excluding individual track lengths; refer to the *supplementary materials*). The high N_s track densities make U zoning on the etched grain surface easily detectable, and none of the examples showed evidence for strong zonation. One procedural difference for the data discussed here is that the AFT samples were analyzed in two separate aliquots (dated "blind") with a focus on collecting more track length data. For the second aliquot, lengths were only measured from grains where tracks were counted for age determination—this was done to test for possible multikinetic behavior and to facilitate direct linking of measured lengths with apparent ages (for example Issler and others, 2022).

Electron Probe Microanalysis

Electron probe microanalysis (EPMA) was carried out using a JEOL JXA8500F field emission electron microprobe with an electron beam size of 5 μm operated at 15 kV (current 20 nA) for a single-spot per grain on the AFT mounts at the Washington State University GeoAnalytical Laboratory. The analyzed elements included: Ca, P, F, Cl, Na, Mg, Mn, Fe, Sr, Y, La, Ce, S, and OH estimated by difference using the same methods discussed in McDannell and others (2019a). The second AFT aliquots included Si and had two EPMA spots analysed, one near the laser-ablation pit, and the other located in a different area of the grain to assess potential compositional heterogeneity (fig. 4). Complete EPMA data are provided in the *supplementary materials* and are summarized in table 1, table 2, and table 3. The apatite stoichiometric calculations for EPMA data from Ketcham (2015) were used to calculate weight percent oxide totals (and atoms per formula unit; apfu) including OH and F-Cl oxygen-equivalent

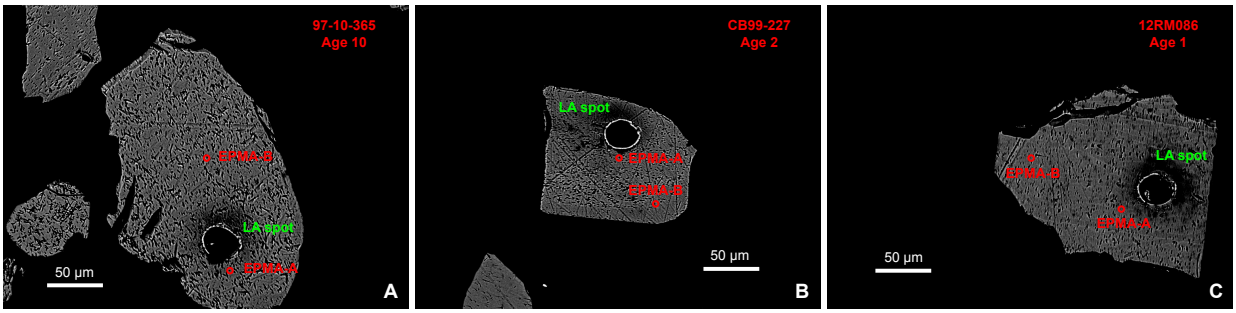

Fig. 4. Electron backscatter images of EPMA single-spot analyses for representative aliquot-2 apatite grains from the fission-track mounts. Intra-grain compositional heterogeneity is present but minor. Spot analyses were 5 μm in diameter. Spot-A was analyzed near the laser ablation spot and spot-B was randomly collected in another location. (A) The eCl values for sample 97-10-365 grain-age-10 (a2-10) are 0.008 apfu (spot A; r_{mr0} = 0.838; equivalent D_{par} = 1.78 μm) and 0.000 apfu (spot B; r_{mr0} = 0.840; eD_{par} = 1.75 μm). (B) The eCl values for sample CB99-227 grain-age-2 (a2-2) are 0.018 apfu (spot A; r_{mr0} = 0.834; eD_{par} = 1.81 μm) and 0.025 apfu (spot B; r_{mr0} = 0.832; eD_{par} = 1.83 μm). Spot-B is near the grain edge where there is a narrow band (10–15 μm) of modest U zoning that is visible due to the lower spontaneous track density compared to the grain interior. (C) The eCl values for sample 12RM086 grain-age-1 (a2-1) are 0.006 apfu (spot A; r_{mr0} = 0.838; eD_{par} = 1.77 μm) and 0.014 apfu (spot B; r_{mr0} = 0.835; eD_{par} = 1.80 μm). The r_{mr0} values were calculated using the Carlson and others (1999) equations.

corrections. Elemental wt% oxide totals are 98.9 ± 1.9% for 350 analyses (including OH estimation) and suggest near endmember fluorapatite or secondary mixed F-Cl-OH apatite with secondary trace element and REE presence in all three samples. Estimated grain average wt.% oxide elements include (aliquot-2 data only): Ca = ~54.7%, P = ~41%, F = ~3.0%, OH = ~0.55%, Si = ~0.14%, Y = ~0.1%, S = ~0.09%, Mn = ~0.06%, Sr = ~0.05%, Na = ~0.05%, Ce = ~0.04%, Cl = ~0.02%, and Fe = ~0.02%. The aliquot-2 grains with multiple probe spots indicated insignificant-to-moderate variation in composition, suggesting intra-grain elemental zoning is present in all of the samples but it is not extreme. The few grains with low totals < 97% are flagged in the supplemental dataset and should be used with caution for any petrogenetic interpretation (refer to discussion in Issler and others, 2022). The elemental data were plugged into the multivariate equation of Carlson and others (1999) to calculate a single kinetic parameter, r_{mr0}, to approximate the annealing kinetics of the AFT data during inverse modelling. The nonlinear r_{mr0} values were also converted to linear "effective Cl" (eCl) values (see McDannell & Issler, 2021 and Issler and others, 2022 for discussion). Effective Cl of 0.0 apfu is indicative of endmember fluorapatite and negative eCl values indicate an extrapolation of the Carlson and others (1999) r_{mr0}–Cl relation for r_{mr0} values > 0.84, and imply lower track retentivity compared to common fluorapatite.

LA-ICPMS AFT "Super-Sample" Apparent Ages, Track Lengths, and Elemental Chemistry

The central ages presented in the data tables are calculated from the single-grain LAFT ages and their 1σ uncertainties (the mean of the log-normal distribution of ages; Vermeesch, 2018, 2019). Sample 97-10-365 has an AFT central age of 512 ± 18 Ma (1σ, n = 63, age dispersion = 26%, P(χ^2) = 0.0; table 1) with grain ages spanning 300 ± 39 Ma to 926 ± 328 Ma and a conventional mean track length (MTL) of 12.01 ± 1.75 μm and *c*-axis projected MTL of 13.64 ± 1.02 μm (n = 709). The N_s counts for this sample totaled 14,353 (table 1). The median r_{mr0} is 0.843 and the average eCl is -0.007 ± 0.019 apfu across all probed grains. The absolute difference between the

Table 1. Apatite fission-track data for sample 97-10-365, Hearne Domain (lon/lat: -94.84072244, 59.0724352)

N_s	Area (cm^2)	$^{238}U/^{43}Ca$	1σ	$P_i\Omega_i$	$\sigma P_i^2\Omega_i^2$	AFT age† (Ma)	1σ (Ma)	D_{par} (μm)	F⋆ (apfu)	Cl⋆ (apfu)	OH⋆ (apfu)	r_{mr0} 1999	eCl (A) (apfu)	eCl (B) (apfu)	U–Pb‡ age (Ma)	2σ (Ma)	aliquot grain
97	2.91E-05	2.77E-02	9.38E-03	8.06E-07	7.46E-14	926	328	2.09	1.69	0.00	0.30	0.840	0.001	–	–	–	a1-1
73	2.91E-05	3.01E-02	2.79E-03	8.76E-07	6.60E-15	655	98	1.96	1.55	0.00	0.45	0.843	-0.007	–	–	–	a1-2
80	2.91E-05	4.14E-02	3.23E-03	1.21E-06	8.83E-15	527	72	1.99	1.58	0.01	0.42	0.842	-0.005	–	–	–	a1-3
426	5.82E-05	1.49E-01	9.66E-03	8.65E-06	3.17E-13	395	33	1.71	1.59	0.01	0.40	0.838	0.005	–	–	–	a1-4
162	3.88E-05	7.08E-02	4.49E-03	2.75E-06	3.04E-14	470	48	1.83	1.52	0.00	0.47	0.838	0.008	–	–	–	a1-5
65	2.91E-05	3.69E-02	1.07E-03	1.07E-06	9.79E-16	482	62	1.62	1.59	0.00	0.41	0.840	0.002	–	2155	471	a1-6
94	1.94E-05	4.99E-02	1.72E-03	9.70E-07	1.12E-15	756	83	1.86	–	–	–	–	–	–	–	–	a1-7*
64	2.43E-05	1.67E-01	4.61E-02	4.05E-06	1.25E-12	130	39	1.67	1.60	0.00	0.39	0.845	-0.016	–	–	–	a1-8*
126	3.40E-05	4.73E-02	1.43E-03	1.61E-06	2.37E-15	618	59	1.94	1.71	0.00	0.29	0.844	-0.011	–	2424	561	a1-9
59	1.94E-05	5.24E-02	3.44E-03	1.02E-06	4.45E-15	463	68	1.98	1.63	0.01	0.37	0.845	-0.016	–	2479	1347	a1-10
264	3.11E-05	1.85E-01	4.20E-03	5.73E-06	1.70E-14	370	25	1.97	1.58	0.11	0.31	0.814	0.071	–	2400	299	a1-11
104	4.85E-05	4.14E-02	1.09E-03	2.01E-06	2.79E-15	415	43	1.97	1.62	0.01	0.37	0.842	-0.005	–	2321	413	a1-12
149	3.40E-05	3.06E-02	7.03E-04	1.04E-06	5.70E-16	1087	94	1.86	1.69	0.00	0.31	0.849	-0.027	–	1980	324	a1-13
45	2.33E-05	2.83E-02	6.74E-04	6.59E-07	2.46E-16	541	82	1.88	1.77	0.01	0.22	0.853	-0.038	–	1995	419	a1-14
106	2.91E-05	6.24E-02	1.45E-03	1.82E-06	1.79E-15	466	47	1.93	1.65	0.00	0.35	0.845	-0.014	–	2385	402	a1-15
124	3.88E-05	5.28E-02	1.20E-03	2.05E-06	2.17E-15	482	45	1.88	1.73	0.00	0.26	0.844	-0.012	–	2080	364	a1-16
118	2.43E-05	5.32E-02	1.39E-03	1.29E-06	1.14E-15	715	70	2.04	1.60	0.00	0.40	0.844	-0.012	–	2464	498	a1-17
103	2.43E-05	3.65E-02	1.02E-03	8.86E-07	6.09E-16	896	93	2.08	1.62	0.01	0.37	0.846	-0.017	–	2107	477	a1-18
101	3.40E-05	3.95E-02	9.96E-04	1.34E-06	1.14E-15	595	62	1.82	1.62	0.01	0.38	0.841	-0.002	–	2526	460	a1-19
54	2.91E-05	3.89E-02	1.44E-03	1.13E-06	1.75E-15	382	54	1.65	1.69	0.00	0.31	0.847	-0.021	–	2497	596	a1-20
97	2.91E-05	3.03E-02	1.40E-03	8.83E-07	1.66E-15	850	96	2.14	1.65	0.01	0.35	0.840	0.000	–	–	–	a1-21
81	2.33E-05	2.66E-02	1.27E-03	6.19E-07	8.73E-16	1001	122	1.80	1.50	0.02	0.48	0.827	0.038	–	–	–	a1-22
345	4.37E-05	1.39E-01	3.39E-03	6.06E-06	2.20E-14	455	28	2.03	1.76	0.00	0.24	0.848	-0.023	–	–	–	a1-23
164	4.85E-05	4.80E-02	1.49E-03	2.33E-06	5.25E-15	558	48	1.75	1.57	0.00	0.43	0.844	-0.010	–	–	–	a1-24
96	3.40E-05	5.01E-02	1.73E-03	1.70E-06	3.45E-15	450	49	2.03	–	–	–	–	–	–	2471	593	a1-25
293	3.88E-05	1.50E-01	4.43E-03	5.82E-06	2.95E-14	404	27	1.99	–	–	–	–	–	–	2238	328	a2-1
472	5.82E-05	7.83E-02	2.54E-03	4.56E-06	2.19E-14	804	47	1.86	1.55	0.00	0.45	0.838	0.006	0.006	2205	518	a2-2
446	5.82E-05	1.20E-01	2.84E-03	6.98E-06	2.73E-14	508	28	1.43	–	–	–	–	–	–	1736	383	a2-3
304	5.82E-05	5.22E-02	9.33E-04	3.04E-06	2.95E-15	779	49	1.79	1.52	0.01	0.471	0.841	-0.002	0.000	2193	384	a2-4
228	5.82E-05	5.86E-02	1.15E-03	3.41E-06	4.48E-15	531	38	1.70	1.65	0.01	0.35	0.841	-0.001	-0.001	2088	528	a2-5
274	2.91E-05	1.64E-01	3.12E-03	4.77E-06	8.24E-15	458	30	2.06	1.51	0.01	0.48	0.839	0.003	0.028	2242	376	a2-6
137	3.88E-05	7.85E-02	1.58E-03	3.05E-06	3.76E-15	362	32	1.61	1.68	0.00	0.31	0.848	-0.025	-0.029	1724	305	a2-7
446	4.85E-05	1.80E-01	2.99E-03	8.73E-06	2.10E-14	409	22	1.53	1.71	0.00	0.28	0.850	–	-0.029	2172	249	a2-8
119	3.40E-05	4.78E-02	1.42E-03	1.63E-06	2.33E-15	579	57	1.60	1.62	0.02	0.37	0.842	-0.006	-0.004	2134	307	a2-9
255	4.85E-05	7.41E-02	1.48E-03	3.59E-06	5.15E-15	562	38	1.72	1.66	0.01	0.33	0.837	0.008	0.000	2075	297	a2-10
104	3.88E-05	3.81E-02	9.23E-04	1.48E-06	1.28E-15	557	57	2.02	1.55	0.01	0.44	0.835	0.015	-0.021	1949	356	a2-11
511	5.82E-05	1.82E-01	3.68E-03	1.06E-05	4.59E-14	387	20	1.70	1.69	0.01	0.30	0.848	-0.023	0.018	2292	319	a2-12
699	7.77E-05	1.59E-01	3.33E-03	1.24E-05	6.69E-14	452	21	1.88	1.51	0.00	0.49	0.839	0.003	-0.002	2176	312	a2-13
216	2.91E-05	1.06E-01	2.36E-03	3.08E-06	4.72E-15	555	41	1.54	1.79	0.01	0.20	0.844	-0.010	0.014	2236	447	a2-14
61	3.88E-05	4.24E-02	9.62E-04	1.65E-06	1.39E-15	300	39	1.72	1.71	0.00	0.28	0.848	-0.024	-0.017	2126	646	a2-15
210	4.85E-05	7.83E-02	1.72E-03	3.80E-06	6.96E-15	442	33	1.79	1.52	0.00	0.48	0.837	0.011	-0.012	1427	347	a2-16
452	4.85E-05	2.09E-01	4.77E-03	1.01E-05	5.35E-14	359	20	1.60	1.52	0.01	0.48	0.832	0.024	-0.021	1674	273	a2-17
248	3.49E-05	1.34E-01	2.54E-03	4.68E-06	7.86E-15	424	29	1.70	1.57	0.01	0.42	0.843	-0.007	-0.024	1527	275	a2-18
155	4.37E-05	8.41E-02	1.68E-03	3.68E-06	5.39E-15	340	29	1.56	1.58	0.01	0.41	0.842	-0.005	0.001	1852	381	a2-19
252	2.91E-05	1.51E-01	2.46E-03	4.39E-06	5.12E-15	458	31	1.77	1.63	0.07	0.30	0.828	0.035	-0.027	1759	219	a2-20
146	3.88E-05	4.94E-02	1.57E-03	1.92E-06	3.71E-15	601	54	1.93	1.56	0.01	0.43	0.842	-0.006	-0.022	1863	541	a2-21
474	5.82E-05	1.32E-01	3.36E-03	7.68E-06	3.82E-14	491	27	1.57	1.56	0.00	0.43	0.839	0.004	-0.017	2123	504	a2-22
141	3.40E-05	4.14E-02	1.58E-03	1.41E-06	2.89E-15	780	73	1.51	1.59	0.00	0.41	0.838	0.006	-0.039	2213	743	a2-23
236	7.77E-05	3.56E-02	1.32E-03	2.77E-06	1.05E-14	670	51	1.53	1.68	0.00	0.32	0.850	-0.028	-0.021	1521	518	a2-24
390	4.85E-05	1.82E-01	4.09E-03	8.83E-06	3.93E-14	356	21	1.61	1.71	0.01	0.29	0.828	0.035	-0.026	2079	261	a2-25
576	5.82E-05	1.95E-01	4.71E-03	1.13E-05	7.51E-14	407	21	1.61	1.79	0.01	0.20	0.851	-0.032	0.000	2157	331	a2-26
213	5.82E-05	5.31E-02	1.52E-03	3.09E-06	7.83E-15	546	42	1.81	1.50	0.01	0.50	0.839	0.004	0.000	2383	632	a2-27
166	5.82E-05	4.07E-02	1.02E-03	2.37E-06	3.52E-15	555	46	1.63	1.58	0.01	0.41	0.842	-0.006	-0.007	2121	566	a2-28
496	4.85E-05	2.08E-01	6.17E-03	1.01E-05	8.95E-14	394	22	1.65	1.57	0.01	0.42	0.843	-0.009	-0.025	1828	331	a2-29
151	4.37E-05	4.53E-02	1.16E-03	1.98E-06	2.57E-15	602	52	1.68	1.52	0.00	0.47	0.831	0.027	0.006	2199	551	a2-30
378	4.85E-05	1.35E-01	3.42E-03	6.55E-06	2.75E-14	461	28	1.90	1.76	0.00	0.24	0.852	-0.036	-0.019	1468	268	a2-31
126	3.88E-05	5.49E-02	2.02E-03	2.13E-06	6.14E-15	472	46	1.57	1.75	0.00	0.25	0.851	-0.034	-0.015	2164	659	a2-32
420	4.85E-05	1.15E-01	2.45E-03	5.58E-06	1.41E-14	595	33	1.67	1.57	0.01	0.43	0.836	0.013	0.008	2311	397	a2-33
358	4.85E-05	7.63E-02	1.91E-03	3.70E-06	8.58E-15	754	46	1.67	1.59	0.01	0.40	0.841	–	-0.002	1763	395	a2-34
193	3.40E-05	1.23E-01	2.53E-03	4.18E-06	7.40E-15	371	28	1.66	1.66	0.00	0.34	0.842	-0.006	-0.009	2042	417	a2-35
137	3.40E-05	4.75E-02	1.10E-03	1.62E-06	1.40E-15	666	60	1.50	1.60	0.01	0.39	0.835	0.014	0.003	2268	558	a2-36
306	3.88E-05	1.33E-01	3.15E-03	5.16E-06	1.49E-14	473	30	1.60	1.78	0.00	0.22	0.848	-0.023	-0.016	1867	269	a2-37
86	3.11E-05	4.56E-02	9.85E-04	1.42E-06	9.38E-16	483	54	1.54	1.77	0.01	0.23	0.847	-0.021	-0.006	2386	515	a2-38
338	4.85E-05	1.45E-01	2.34E-03	7.03E-06	1.29E-14	386	23	1.56	1.69	0.00	0.31	0.849	-0.028	-0.031	1470	213	a2-39
101	3.40E-05	5.79E-02	1.19E-03	1.97E-06	1.64E-15	411	42	1.71	1.62	0.01	0.37	0.836	0.013	-0.021	2304	469	a2-40
14353	2.61E-03			2.40E-04	1.20E-12	512	18	1.77	1.63	0.01	0.36	0.842	-0.004	-0.010	2075	67	

N_s = spontaneous track count; P_i = down-pit weighted $^{238}U/^{43}Ca$; Ω_i = track count area

†AFT single-grain ages are calculated using the LA-ICPMS (ζ-calibration) method with modified ζ = 8.2727, standard error (ζ) = 0.1407 and ^{238}U total decay constant of 1.55125×10^{-10} yr^{-1}. Bottom table row displays the analysis sums, AFT central age ± 1σ error, and the mean values for the tabulated elements/kinetic parameters. Aliquot grains marked with an asterisk experienced analysis failure from blowout during lasing and are omitted from summary calculations but are reported for completeness; see discussion in Issler and others, 2022.

⋆Average values reported for F, Cl, OH, D_{par}, and effective Cl (eCl) in bottom row, median value shown for r_{mr0}; Individual grain D_{par} values are the mean of 4 measurements. Aliquot-2 had two EPMA probe spots, one near the AFT laser ablation pit (A) and another elsewhere on the grain (B) to assess compositional heterogeneity. Elemental data for aliquot-2 (F, Cl, OH, r_{mr0}) are only reported in the table for spot A. Average wt % oxide total for aliquot-2 replicates is 97.4 ± 1.8%; median = 98% (n = 74).

‡Individual U–Pb dates are common Pb-corrected isotopic sums. Summary U–Pb date of 2075 ± 67 Ma in the table is the weighted mean of individual dates (2σ, n = 49/53, MSWD = 1.51, P(χ^2) = 0.013). The weighted mean $^{207}Pb/^{206}Pb$ date calculated in IsoplotR (Vermeesch, 2018) using $^{238}U/^{206}Pb$ and $^{207}Pb/^{206}Pb$ isotopic ratios is 2173 ± 72 Ma (2σ with overdispersion, n = 53/53, MSWD = 1.8, P(χ^2) = 0.00).

Table 2. Apatite fission-track data for sample CB99-227, Trans-Hudson Orogen (lon/lat: -94.96948441, 56.46946203)

N_s	Area (cm^2)	$^{238}U/^{43}Ca$	1σ	$P_i\Omega_i$	$\sigma P_i^2\Omega_i^2$	AFT age† (Ma)	1σ (Ma)	D_{par} (μm)	F⋆ (apfu)	Cl⋆ (apfu)	OH⋆ (apfu)	r_{mr0} 1999	eCl (A) (apfu)	eCl (B) (apfu)	U–Pb‡ age (Ma)	2σ (Ma)	aliquot grain
461	5.82E-05	1.33E-01	2.97E-03	7.77E-06	2.98E-14	473	26	2.09	1.65	0.01	0.34	0.848	-0.022	–	1526	208	a1-1
175	3.88E-05	4.07E-02	2.14E-03	1.58E-06	6.88E-15	856	80	1.91	1.55	0.01	0.44	0.838	0.008	–	1471	319	a1-2
367	5.82E-05	8.80E-02	1.97E-03	5.12E-06	1.32E-14	567	34	2.16	–	–	–	–	–	–	1581	221	a1-3
131	2.91E-05	7.94E-02	1.85E-03	2.31E-06	2.91E-15	452	42	2.16	1.69	0.01	0.30	0.848	-0.025	–	1559	152	a1-4
257	9.71E-05	3.00E-02	6.97E-04	2.91E-06	4.57E-15	692	48	2.16	1.61	0.01	0.38	0.843	-0.009	–	1621	293	a1-5
241	5.82E-05	6.46E-02	1.74E-03	3.76E-06	1.02E-14	509	37	2.20	1.53	0.01	0.46	0.841	-0.001	–	1572	213	a1-6
72	3.88E-05	2.42E-02	5.89E-04	9.38E-07	5.23E-16	606	74	2.12	1.53	0.01	0.46	0.837	0.011	–	1605	301	a1-7
211	4.85E-05	3.83E-02	8.69E-04	1.86E-06	1.78E-15	878	65	1.59	1.74	0.01	0.25	0.851	-0.033	–	1541	219	a1-8
103	4.85E-05	2.99E-02	7.08E-04	1.45E-06	1.18E-15	562	58	2.10	1.50	0.01	0.49	0.835	0.016	–	1582	323	a1-9
197	5.82E-05	3.77E-02	9.32E-04	2.20E-06	2.95E-15	703	54	2.25	1.67	0.02	0.31	0.838	0.007	–	1528	281	a1-10
71	3.88E-05	1.98E-02	7.41E-04	7.70E-07	8.27E-16	721	91	1.80	1.59	0.01	0.39	0.837	0.011	–	1433	566	a1-11
438	5.82E-05	9.98E-02	3.01E-03	5.81E-06	3.08E-14	595	35	1.89	1.59	0.01	0.39	0.833	0.022	–	1516	261	a1-12
153	4.37E-05	5.64E-02	1.22E-03	2.46E-06	2.83E-15	494	42	2.22	1.64	0.01	0.35	0.846	-0.019	–	1596	219	a1-13
334	6.21E-05	5.62E-02	1.37E-03	3.49E-06	7.22E-15	746	46	2.07	1.73	0.01	0.26	0.851	-0.034	–	1541	234	a1-14
343	7.77E-05	3.51E-02	1.24E-03	2.73E-06	9.29E-15	965	64	2.22	1.64	0.01	0.35	0.847	-0.021	–	1485	374	a1-15
615	5.82E-05	2.29E-01	4.70E-03	1.34E-05	7.51E-14	370	18	1.64	1.53	0.01	0.47	0.836	0.013	0.026	1722	285	a2-1
714	5.82E-05	2.18E-01	4.38E-03	1.27E-05	6.51E-14	449	21	1.70	1.43	0.01	0.56	0.834	0.018	0.025	1661	219	a2-2
103	3.98E-05	3.87E-02	6.06E-03	1.54E-06	5.82E-14	530	99	2.16	1.60	0.01	0.39	0.837	0.010	–	–	–	a2-3
218	9.71E-05	8.79E-02	3.06E-03	8.53E-06	8.80E-14	208	16	1.74	1.45	0.01	0.54	0.837	0.010	0.036	–	–	a2-4
114	4.37E-05	4.08E-02	1.90E-03	1.78E-06	6.91E-15	509	54	1.43	1.59	0.01	0.41	0.835	0.015	-0.023	–	–	a2-5
118	9.71E-05	2.15E-02	1.73E-03	2.09E-06	2.82E-14	452	56	1.54	1.51	0.01	0.48	0.839	0.003	0.013	–	–	a2-6
138	5.82E-05	4.77E-02	9.40E-04	2.78E-06	3.00E-15	399	35	1.63	1.60	0.01	0.40	0.835	0.017	-0.021	1626	478	a2-7
80	4.37E-05	3.91E-02	8.71E-03	1.71E-06	1.45E-13	376	94	1.41	–	–	–	–	–	–	–	–	a2-8
145	4.85E-05	2.88E-02	7.38E-04	1.40E-06	1.28E-15	806	71	1.49	1.55	0.00	0.45	0.842	-0.006	0.001	1631	607	a2-9
384	2.91E-05	3.37E-01	6.10E-03	9.81E-06	3.15E-14	316	18	1.68	1.57	0.01	0.42	0.837	0.009	0.025	1593	195	a2-10
472	4.85E-05	1.95E-01	3.91E-03	9.47E-06	3.61E-14	400	21	1.79	1.45	0.01	0.55	0.832	0.024	0.016	1635	232	a2-11
294	6.79E-05	5.78E-02	1.41E-03	3.92E-06	9.20E-15	592	39	2.16	1.52	0.02	0.46	0.833	0.020	0.028	1624	426	a2-12
440	4.85E-05	1.67E-01	3.35E-03	8.11E-06	2.65E-14	434	24	1.89	1.52	0.02	0.46	0.833	0.022	0.017	1615	289	a2-13
128	4.85E-05	4.35E-02	1.25E-03	2.11E-06	3.67E-15	483	46	1.89	1.69	0.01	0.30	0.849	-0.026	0.010	1560	421	a2-14
324	9.71E-05	5.34E-02	1.42E-03	5.19E-06	1.89E-14	497	32	1.87	1.68	0.01	0.31	0.848	-0.022	0.017	1547	661	a2-15
119	4.85E-05	3.60E-02	1.23E-03	1.75E-06	3.57E-15	541	54	1.64	–	–	–	–	–	–	1548	535	a2-16
404	4.85E-05	1.25E-01	3.01E-03	6.05E-06	2.14E-14	530	31	1.71	1.49	0.01	0.50	0.841	-0.001	-0.022	1473	324	a2-17
195	5.82E-05	6.32E-02	1.57E-03	3.68E-06	8.35E-15	424	33	1.71	1.61	0.01	0.38	0.837	0.011	-0.003	1641	418	a2-18
234	4.85E-05	6.93E-02	2.43E-03	3.37E-06	1.39E-14	551	42	1.72	1.51	0.02	0.48	0.831	0.028	0.018	–	–	a2-19
242	5.82E-05	7.26E-02	2.72E-03	4.23E-06	2.50E-14	457	35	1.65	1.52	0.01	0.46	0.836	0.012	-0.013	–	–	a2-20
203	2.91E-05	1.50E-01	7.94E-03	4.37E-06	5.35E-14	373	33	1.77	1.52	0.01	0.47	0.834	0.018	0.008	–	–	a2-21
140	3.88E-05	5.66E-02	2.68E-03	2.20E-06	1.08E-14	507	50	1.60	1.57	0.01	0.43	0.837	0.011	0.006	–	–	a2-22
555	5.82E-05	1.55E-01	4.73E-03	9.05E-06	7.59E-14	488	27	2.03	1.58	0.01	0.42	0.845	-0.016	0.003	–	–	a2-23
129	4.85E-05	4.29E-02	1.45E-03	2.08E-06	4.96E-15	493	47	1.56	1.60	0.01	0.39	0.839	0.005	-0.001	–	–	a2-24
84	4.85E-05	1.98E-02	1.35E-03	9.59E-07	4.30E-15	687	89	1.72	1.57	0.01	0.42	0.838	0.008	0.045	–	–	a2-25
300	4.85E-05	1.70E-01	3.69E-03	8.23E-06	3.21E-14	295	19	1.77	1.56	0.01	0.43	0.843	-0.009	0.009	–	–	a2-26
316	4.85E-05	9.24E-02	2.09E-03	4.49E-06	1.03E-14	558	35	1.73	1.46	0.01	0.53	0.839	0.004	-0.001	1637	292	a2-27
222	5.82E-05	1.02E-01	2.14E-03	5.95E-06	1.56E-14	301	22	1.47	1.72	0.00	0.28	0.840	0.000	-0.029	–	–	a2-28
238	2.91E-05	2.18E-01	4.37E-03	6.34E-06	1.62E-14	303	21	2.11	1.58	0.01	0.42	0.842	-0.004	0.038	1665	221	a2-29
63	3.88E-05	3.33E-02	1.76E-03	1.29E-06	4.69E-15	391	54	1.43	1.71	0.01	0.28	0.843	-0.009	-0.041	–	–	a2-30
195	4.85E-05	8.53E-02	2.19E-03	4.14E-06	1.13E-14	378	29	2.17	1.47	0.01	0.52	0.835	0.015	-0.013	1736	430	a2-31
248	4.85E-05	7.39E-02	1.99E-03	3.59E-06	9.34E-15	548	39	1.51	1.47	0.01	0.52	0.836	0.011	0.001	1546	396	a2-32
290	5.82E-05	1.22E-01	3.49E-03	7.09E-06	4.14E-14	330	22	1.72	1.62	0.02	0.36	0.840	-0.001	0.007	1504	250	a2-33
98	2.91E-05	6.77E-02	2.12E-03	1.97E-06	3.80E-15	399	43	1.66	1.95	0.01	0.04	0.856	-0.048	0.030	1614	279	a2-34
328	3.88E-05	2.15E-01	5.78E-03	8.34E-06	5.04E-14	317	20	1.92	1.51	0.01	0.48	0.839	0.003	-0.001	1753	304	a2-35
12444	2.63E-03			2.19E-04	1.14E-12	486	22	1.83	1.58	0.01	0.41	0.838	0.001	0.007	1585	46	

N_s = spontaneous track count; P_i = down-pit weighted $^{238}U/^{43}Ca$; Ω_i = track count area

†AFT single-grain ages are calculated using the LA-ICPMS (ζ-calibration) method with modified ζ = 8.2727, standard error (ζ) = 0.1407 and ^{238}U total decay constant of 1.55125×10^{-10} yr^{-1}. Bottom table row displays the analysis sums, AFT central age ± 1σ error, and the mean values for the tabulated elements/kinetic parameters.

⋆Average values reported for F, Cl, OH, D_{par}, and effective Cl (eCl) in bottom row, median value shown for r_{mr0}; Individual grain D_{par} values are the mean of 4 measurements. Aliquot-2 had two EPMA probe spots, one near the AFT laser ablation pit and another elsewhere on the grain to assess compositional heterogeneity. Elemental data for aliquot-2 (F, Cl, OH, r_{mr0}) are only reported in the table for spot A. Average wt % oxide total for aliquot-2 replicates is 99.6 ± 1.2%; median = 99.7% (n = 65).

‡Individual U–Pb dates are common Pb-corrected isotopic sums. Summary U–Pb date of 1585 ± 46 Ma in the table is the weighted mean of individual dates (2σ, n = 35/35, MSWD = 0.22, P(χ^2) = 1). The weighted mean $^{207}Pb/^{206}Pb$ date calculated in IsoplotR (Vermeesch, 2018) using $^{238}U/^{206}Pb$ and $^{207}Pb/^{206}Pb$ isotopic ratios is 1603 ± 72 Ma (2σ, n = 35/35, MSWD = 0.13, P(χ^2) = 1).

Table 3. Apatite fission-track data for sample 12RM086, western Superior Province (lon/lat: -86.9604038, 52.874674)

N_s	Area (cm^2)	$^{238}U/^{43}Ca$	1σ	$P_i\Omega_i$	$\sigma P_i^2\Omega_i^2$	AFT age† (Ma)	1σ (Ma)	D_{par} (μm)	F⋆ (apfu)	Cl⋆ (apfu)	OH⋆ (apfu)	r_{mr0} 1999	eCl (A) (apfu)	eCl (B) (apfu)	U–Pb‡ age (Ma)	2σ (Ma)	aliquot grain
350	6.79E-05	7.41E-02	7.58E-03	5.03E-06	2.65E-13	551	64	2.25	1.66	0.00	0.34	0.846	-0.017	–	–	–	a1-1
146	4.85E-05	6.33E-02	5.34E-03	3.07E-06	6.72E-14	382	46	2.02	1.73	0.00	0.26	0.845	-0.013	–	–	–	a1-2
252	9.71E-05	2.65E-02	1.81E-02	2.57E-06	3.09E-12	763	523	2.17	1.68	0.00	0.32	0.847	-0.021	–	2288	1013	a1-3
111	2.91E-05	6.16E-02	5.81E-03	1.79E-06	2.86E-14	493	66	1.94	1.83	0.00	0.17	0.847	-0.020	–	–	–	a1-4
196	4.85E-05	1.01E-01	7.43E-03	4.90E-06	1.30E-13	323	34	1.80	1.81	0.00	0.19	0.850	-0.031	–	–	–	a1-5
51	1.46E-05	4.07E-02	2.25E-03	5.92E-07	1.07E-15	676	102	2.39	1.77	0.00	0.23	0.849	-0.027	–	–	–	a1-6
64	2.04E-05	3.43E-02	3.06E-03	6.99E-07	3.89E-15	716	111	2.00	1.79	0.00	0.21	0.852	-0.037	–	–	–	a1-7
174	6.21E-05	7.10E-02	5.83E-03	4.41E-06	1.31E-13	319	36	1.78	1.86	0.00	0.14	0.854	-0.041	–	–	–	a1-8
128	4.37E-05	5.86E-02	4.04E-03	2.56E-06	3.11E-14	401	45	1.98	1.97	0.00	0.03	0.860	-0.063	–	–	–	a1-9
85	3.88E-05	4.22E-02	2.93E-03	1.64E-06	1.30E-14	416	54	1.95	1.78	0.00	0.22	0.852	-0.035	–	–	–	a1-10
63	1.55E-05	5.63E-02	2.96E-03	8.74E-07	2.11E-15	570	78	1.89	1.80	–	–	–	–	–	–	–	a1-11
204	5.82E-05	7.58E-02	4.15E-03	4.41E-06	5.85E-14	371	34	1.88	1.70	0.00	0.20	0.846	-0.017	–	–	–	a1-12
119	3.40E-05	4.58E-02	2.85E-03	1.56E-06	9.39E-15	603	68	2.14	1.78	0.00	0.30	0.840	0.002	–	–	–	a1-13
51	2.43E-05	4.39E-02	4.05E-03	1.07E-06	9.65E-15	384	65	1.97	1.72	0.00	0.22	0.852	-0.036	–	–	–	a1-14
167	4.85E-05	4.47E-02	1.69E-03	2.17E-06	6.73E-15	607	53	1.88	1.85	0.01	0.27	0.842	-0.006	–	2251	585	a1-15
79	3.11E-05	5.30E-02	1.93E-03	1.65E-06	3.58E-15	385	46	2.25	1.80	0.00	0.15	0.856	-0.048	–	–	–	a1-16
53	4.85E-05	1.55E-02	5.80E-04	7.53E-07	7.93E-16	557	80	2.04	1.71	0.00	0.20	0.844	-0.012	–	–	–	a1-17
128	4.85E-05	4.14E-02	1.20E-03	2.01E-06	3.39E-15	506	48	2.16	1.77	0.00	0.29	0.847	-0.020	–	2323	552	a1-18
65	2.33E-05	6.97E-02	1.72E-03	1.62E-06	1.61E-15	323	41	1.88	1.76	0.01	0.23	0.845	-0.015	–	2366	263	a1-19
358	9.71E-05	5.06E-02	1.12E-03	4.91E-06	1.18E-14	577	34	1.86	1.73	0.00	0.24	0.845	-0.016	–	2256	357	a1-20
142	3.88E-05	6.23E-02	1.32E-03	2.42E-06	2.63E-15	468	41	1.81	1.61	0.00	0.27	0.850	-0.031	–	2347	313	a1-21
105	3.88E-05	4.14E-02	9.70E-04	1.61E-06	1.42E-15	519	53	2.12	1.67	0.00	0.38	0.841	-0.002	–	2308	372	a1-22
159	4.85E-05	3.37E-02	8.06E-04	1.64E-06	1.53E-15	758	64	2.19	1.67	0.00	0.33	0.846	-0.016	–	2440	430	a1-23
53	4.85E-05	1.79E-02	4.65E-04	8.71E-07	5.09E-16	485	68	2.04	1.73	0.00	0.33	0.848	-0.024	–	2028	410	a1-24
140	4.85E-05	4.29E-02	1.04E-03	2.08E-06	2.56E-15	534	48	1.73	–	0.00	0.27	0.835	0.015	–	2150	295	a1-25
210	9.71E-05	3.32E-02	8.12E-04	3.22E-06	6.22E-15	518	39	1.63	1.73	0.00	0.27	0.838	0.006	0.014	2217	784	a2-1
108	4.85E-05	5.49E-02	1.24E-03	2.66E-06	3.62E-15	327	33	1.56	1.81	0.01	0.19	0.840	0.002	-0.018	2402	540	a2-2
144	4.85E-05	6.73E-02	1.38E-03	3.26E-06	4.48E-15	355	31	1.80	1.73	0.00	0.27	0.847	-0.021	-0.021	2343	516	a2-3
68	9.71E-05	1.24E-02	4.07E-04	1.20E-06	1.56E-15	451	57	1.61	1.96	0.01	0.03	0.860	-0.062	-0.029	2122	1126	a2-4
151	4.85E-05	7.10E-02	1.09E-03	3.44E-06	2.79E-15	353	30	1.89	1.66	0.01	0.33	0.843	-0.009	0.008	2304	369	a2-5
268	9.71E-05	4.49E-02	1.06E-03	4.36E-06	1.06E-14	489	33	1.86	1.76	0.00	0.24	0.839	0.003	-0.038	2594	677	a2-6
201	4.85E-05	8.17E-02	1.70E-03	3.96E-06	6.80E-15	407	31	1.87	1.60	0.01	0.40	0.843	-0.009	-0.027	2436	551	a2-7
186	5.82E-05	5.29E-02	1.35E-03	3.08E-06	6.17E-15	481	38	1.64	1.63	0.01	0.36	0.832	0.024	-0.022	2378	617	a2-8
258	5.82E-05	8.73E-02	1.71E-03	5.08E-06	9.90E-15	407	27	1.77	1.66	0.00	0.34	0.845	-0.015	-0.047	2488	471	a2-9
136	4.85E-05	4.95E-02	9.16E-04	2.40E-06	1.97E-15	452	40	1.71	1.76	0.00	0.23	0.851	-0.031	-0.013	2885	1185	a2-10
244	9.71E-05	5.57E-02	1.58E-03	5.41E-06	2.35E-14	363	26	1.68	1.59	0.00	0.41	0.841	-0.003	-0.029	2320	567	a2-11
366	7.77E-05	1.07E-01	2.59E-03	8.31E-06	4.05E-14	354	21	1.89	1.79	0.00	0.21	0.848	-0.025	-0.019	2382	467	a2-12
181	4.85E-05	6.93E-02	1.63E-03	3.36E-06	6.25E-15	431	34	1.74	1.85	0.00	0.15	0.853	-0.038	-0.020	2457	696	a2-13
338	9.71E-05	8.53E-02	1.48E-03	8.28E-06	2.07E-14	329	20	1.84	1.70	0.00	0.29	0.839	0.002	-0.043	2875	587	a2-14
128	4.37E-05	8.12E-02	1.91E-03	3.55E-06	6.97E-15	292	27	1.69	1.80	0.00	0.20	0.851	-0.034	-0.026	2459	515	a2-15
214	9.71E-05	4.11E-02	9.53E-04	3.99E-06	8.56E-15	429	32	1.59	1.81	0.00	0.18	0.845	-0.015	-0.024	2259	897	a2-16
310	5.82E-05	1.05E-01	2.27E-03	6.11E-06	1.75E-14	407	26	1.60	1.66	0.01	0.34	0.844	-0.012	-0.019	2522	414	a2-17
111	4.85E-05	5.28E-02	1.17E-03	2.56E-06	3.22E-15	349	35	1.52	1.83	0.01	0.17	0.848	-0.023	-0.050	2615	656	a2-18
98	4.85E-05	4.07E-02	1.05E-03	1.97E-06	2.59E-15	398	42	1.62	1.85	0.02	0.13	0.842	-0.004	-0.035	2534	797	a2-19
150	7.77E-05	4.47E-02	1.23E-03	3.47E-06	9.13E-15	348	31	1.58	1.76	0.00	0.24	0.846	-0.016	-0.016	2416	667	a2-20
124	3.40E-05	6.08E-02	1.26E-03	2.07E-06	1.84E-15	478	45	1.60	1.82	0.00	0.18	0.852	-0.036	0.006	2322	436	a2-21
131	3.40E-05	9.74E-02	1.94E-03	3.31E-06	4.35E-15	319	29	1.79	1.64	0.02	0.34	0.833	0.022	-0.011	2377	449	a2-22
154	4.85E-05	7.23E-02	1.64E-03	3.51E-06	6.33E-15	353	30	1.71	1.93	0.00	0.07	0.856	-0.049	-0.053	2410	408	a2-23
162	4.85E-05	4.19E-02	1.35E-03	2.03E-06	4.29E-15	628	54	1.69	1.74	0.00	0.26	0.841	-0.003	-0.037	2514	865	a2-24
96	4.85E-05	3.14E-02	1.01E-03	1.52E-06	2.40E-15	501	54	1.53	1.88	0.00	0.11	0.852	-0.036	-0.034	2877	1152	a2-25
71	4.85E-05	2.78E-02	9.36E-04	1.35E-06	2.06E-15	422	52	1.60	1.79	0.00	0.21	0.848	-0.023	-0.030	2314	1047	a2-26
185	4.85E-05	6.79E-02	2.33E-03	3.29E-06	1.28E-14	449	37	1.79	1.70	0.01	0.29	0.837	0.010	-0.060	2563	650	a2-27
99	4.85E-05	2.97E-02	9.94E-04	1.44E-06	2.32E-15	545	58	1.46	1.74	0.00	0.26	0.848	-0.023	-0.033	2737	780	a2-28
171	4.85E-05	6.62E-02	1.35E-03	3.21E-06	4.29E-15	426	35	1.64	1.71	0.00	0.29	0.844	-0.010	-0.031	2457	472	a2-29
95	4.85E-05	3.05E-02	9.04E-04	1.48E-06	1.92E-15	511	55	1.74	1.81	0.01	0.18	0.848	-0.023	-0.041	2738	967	a2-30
198	4.85E-05	4.74E-02	1.11E-03	2.30E-06	2.90E-15	676	52	1.73	1.65	0.01	0.35	0.847	-0.021	-0.019	2381	513	a2-31
147	4.85E-05	5.62E-02	1.14E-03	2.73E-06	3.06E-15	431	37	1.55	1.76	0.00	0.24	0.849	-0.028	-0.039	2334	547	a2-32
154	4.85E-05	8.72E-02	1.61E-03	4.23E-06	6.10E-15	294	25	1.41	1.60	0.00	0.39	0.833	0.021	-0.024	2688	700	a2-33
172	7.77E-05	3.55E-02	9.00E-04	2.76E-06	4.89E-15	496	41	1.75	1.82	0.00	0.18	0.846	-0.018	-0.012	2797	933	a2-34
126	4.85E-05	5.11E-02	1.66E-03	2.48E-06	6.48E-15	407	39	1.75	1.70	0.00	0.30	0.841	-0.002	-0.041	2445	723	a2-35
133	4.85E-05	7.11E-02	2.08E-03	3.45E-06	1.02E-14	311	29	1.61	1.76	0.00	0.24	0.851	-0.033	-0.002	–	–	a2-36
147	4.85E-05	5.64E-02	1.31E-03	2.74E-06	4.04E-15	430	38	1.72	1.84	0.00	0.16	0.848	-0.024	-0.042	2466	742	a2-37
90	2.91E-05	7.48E-02	1.93E-03	2.18E-06	3.15E-15	333	37	1.67	1.72	0.00	0.27	0.846	-0.018	-0.006	2436	443	a2-38
208	4.85E-05	9.69E-02	2.85E-03	4.70E-06	1.91E-14	356	27	1.47	1.72	0.01	0.28	0.847	-0.019	-0.048	2517	592	a2-39
166	4.85E-05	7.72E-02	1.68E-03	3.74E-06	6.64E-15	357	29	1.43	1.79	0.00	0.21	0.851	-0.032	-0.004	2647	630	a2-40
10142	3.42E-03			1.91E-04	4.18E-12	433	12	1.80	1.75	0.00	0.24	0.846	-0.018	-0.026	2387	72	

N_s = spontaneous track count; P_i = down-pit weighted $^{238}U/^{43}Ca$; Ω_i = track count area

†AFT single-grain ages are calculated using the LA-ICPMS (ζ-calibration) method with modified ζ = 8.2727, standard error (ζ) = 0.1407 and ^{238}U total decay constant of 1.55125×10^{-10} yr^{-1}. Bottom table row displays the analysis sums, AFT central age ± 1σ error, and the mean values for the tabulated elements/kinetic parameters.

⋆Average values reported for F, Cl, OH, D_{par}, and effective Cl (eCl) in bottom row, median value shown for r_{mr0}; Individual grain D_{par} values are the mean of 4 measurements. Aliquot-2 had two EPMA probe spots, one near the AFT laser ablation pit (A) and another elsewhere on the grain (B) to assess compositional heterogeneity. Elemental data for aliquot-2 (F, Cl, OH, r_{mr0}) are only reported in the table for spot A. Average wt % oxide total for aliquot-2 replicates is 99.2 ± 1.2%; median = 99% (n = 80).

‡Individual U–Pb dates are common Pb-corrected isotopic sums. Summary U–Pb date of 2387 ± 72 Ma in the table is the weighted mean of individual dates (2σ, n = 49/49, MSWD = 0.38, $P(\chi^2)$ = 1). The weighted mean $^{207}Pb/^{206}Pb$ date calculated in IsoplotR (Vermeesch, 2018) using $^{238}U/^{206}Pb$ and $^{207}Pb/^{206}Pb$ isotopic ratios is 2460 ± 59 Ma (2σ, n = 47/48, MSWD = 0.71, $P(\chi^2)$ = 0.93).

EPMA spot measurements for 37 grains in aliquot-2 ranged from ~0.0–0.06 apfu, with a median value of ~0.02 apfu—this is in agreement with a large suite of analyses from Issler and others (2022) that show most replicate grain eCl measurements are within ~0.03 apfu. The weighted mean apatite $^{207}Pb/^{206}Pb$ date is 2173 ± 72 Ma (2σ; table 1).

The sum of N_s counts was 12,444 for sample CB99-227 with a central age of 486 ± 22 Ma (1σ, n = 50, age dispersion = 30%, P(χ^2) = 0.0; table 2) and grain ages spanning 208 ± 16 Ma to 965 ± 64 Ma. CB99-227 has a measured MTL of 11.81 ± 1.67 μm and *c*-axis projected MTL of 13.54 ± 0.93 μm (n = 656). The median r_{mr0} is 0.839 and the average eCl is 0.001 ± 0.018 apfu across all probed grains. The absolute difference between the EPMA spot measurements for 32 grains in aliquot-2 ranged from ~0.0–0.08 apfu, with a median value of ~0.015 apfu. The weighted mean apatite $^{207}Pb/^{206}Pb$ date is 1603 ± 72 Ma (table 2). Aliquot comparisons for this sample show differences in random grain sampling during analysis. Aliquot-1 contains a dominant proportion of older grains whereas aliquot-2 has a larger proportion of younger, high-U grains—implying there is a greater possibility of sampling bias in studies that report ≤ 20 grain ages.

The Superior Province sample 12RM086 is also a combined dataset, including aliquot-1 that was previously summarized and modelled (McDannell and others, in press; the analytical data are reported here) along with new data for aliquot-2 shown in table 3. We discuss those initial results and interpretations here. Sample 12RM086 was presented with a central AFT age of 484 ± 24 Ma (1σ) and age dispersion of 22% (n = 25). One hundred thirty track lengths were measured with a conventional (unprojected) MTL of 12.67 ± 1.72 μm. McDannell and others (2020 in press) interpreted the first sample aliquot as multikinetic—tentatively exhibiting two kinetic groups with some compositional overlap between populations using the eCl kinetic parameter (complete population overlap using D_{par} and measured Cl). Multikinetic interpretation of 12RM086 was carried out using radial plot mixture modelling (Galbraith & Green, 1990) as a guide for comparing grain chemistry with model age peaks (for example, Issler and others, 2022). Two recognized age peaks of 367 ± 17 Ma and 569 ± 16 Ma were defined during mixture modelling. After sorting grains by eCl (r_{mr0}), the central AFT ages for each kinetic population were determined to be 363 ± 14 Ma and 568 ± 21 Ma, in agreement with those recognized from mixture modelling. Thermal history modelling indicated a thermal maximum of ~75°C in the Devonian at 400 ± 26 Ma (1σ) and a second reheating event with a maximum temperature of ~55°C in the Cretaceous at 76 ± 15 Ma (McDannell and others, in press).

A second aliquot of 12RM086 was dated separately and had many more AFT measurements collected (that is, sum N_s = 6699 and 733 track lengths). This aliquot was also analyzed by EPMA twice on each grain to assess potential elemental variation. The eCl values for both aliquots ranged between -0.063–0.024 apfu (r_{mr0} = 0.859–0.832; n = 125) and the absolute difference between the EPMA spot measurements for all 40 grains in aliquot-2 ranged from ~0.0–0.07 apfu, with a median value of ~0.02 apfu. The second aliquot has a central AFT age of 408 ± 13 Ma (1σ) and a conventional MTL of 12.35 ± 1.81 μm (n = 733)—in general agreement with the results from aliquot-1, with only a minor shift in apparent age and MTL due to greater sampling. The two aliquots were combined into a super-sample (total N_s = 10,142) with a total of 65 grain ages spanning 292 ± 27 Ma to 758 ±

64 Ma. Combined sample 12RM086 has a central age of 433 ± 12 Ma (1σ, n = 65, age dispersion = 21%, P(χ^2) = 0.0; table 3) and a measured MTL of 12.40 ± 1.80 μm and *c*-axis projected MTL of 13.86 ± 1.10 μm (n = 853). The weighted mean apatite $^{207}Pb/^{206}Pb$ date is 2460 ± 59 Ma (table 3).

Multikinetic Cratonic Basement AFT Samples?

An alternative interpretation of the data is that the LAFT super-samples are perhaps represented by a minimum of two kinetic populations identified by radial plot mixture modelling (see Galbraith & Green, 1990; Vermeesch, 2009)—seemingly supported, albeit tenuously, by the apatite chemistry. Mixture modelling of course indicates the presence of multiple model age populations due to the high number of precise LAFT grain ages, which is problematic for determining whether apatite composition is consequential and if discrete age peaks truly exist. The data may be explained in some cases by continuous age distributions rather than the typically assumed discrete age components (Vermeesch, 2019). The presence of multiple kinetic populations (with some overlap) cannot be entirely ruled out when considering the duplicate EPMA measurements and associated eCl (r_{mr0}) for the second AFT aliquots (fig. 5). Kinetic population separation is evident if both EPMA spots are considered in the context of whether age grains fall into the more or less retentive kinetic population from the radial plot mixtures (that is, by utilizing the minimum or maximum eCl value for each grain). This is best observed in sample 97-10-365. The eCl values calculated from the EPMA data collected near the laser ablation pit (spot A) typically indicate complete kinetic population overlap for each super-sample, or display a near continuum of single-grain apparent ages that correlate with apatite composition (relationships cannot be distinguished at all using measured Cl or D_{par}). A continuum is observed in samples CB99-227 and 12RM086.

An implication of these relationships is that the r_{mr0} value derived from a single EPMA spot may not be representative if there is significant intra-grain chemical variation. This indicates that it is plausible for discreet multikinetic AFT populations to be present in cratonic basement samples due to small variations in apatite composition, that are at or beyond the resolution of r_{mr0}. This sort of relationship may be expressed in rocks that experienced slow cooling and moderate thermal annealing. Nevertheless the eCl values for the putative kinetic populations appear to span a narrow kinetic range, which may not be consequential with respect to modelling. However, a complicating, if not obscurant factor is that track annealing behavior (Ketcham and others, 1999, 2007) is poorly constrained beyond common fluorapatite (average eCl of ~0.0–0.05 apfu; Issler and others, 2022). Thus the total degree of separation between apparent kinetic groups explained by the r_{mr0}/eCl parameter is probably underestimated, especially for negative eCl values.

Statistical Evaluation of LAFT Data

We present a large quantity of AFT analytical data that is far beyond what is reported in most studies. The N_s counts alone for our three samples totalled nearly 36,950 and the number of measured track lengths was 2,228—for comparison, each LAFT example represents up to ~2–10× the number of counts and ~6–8× the number of lengths

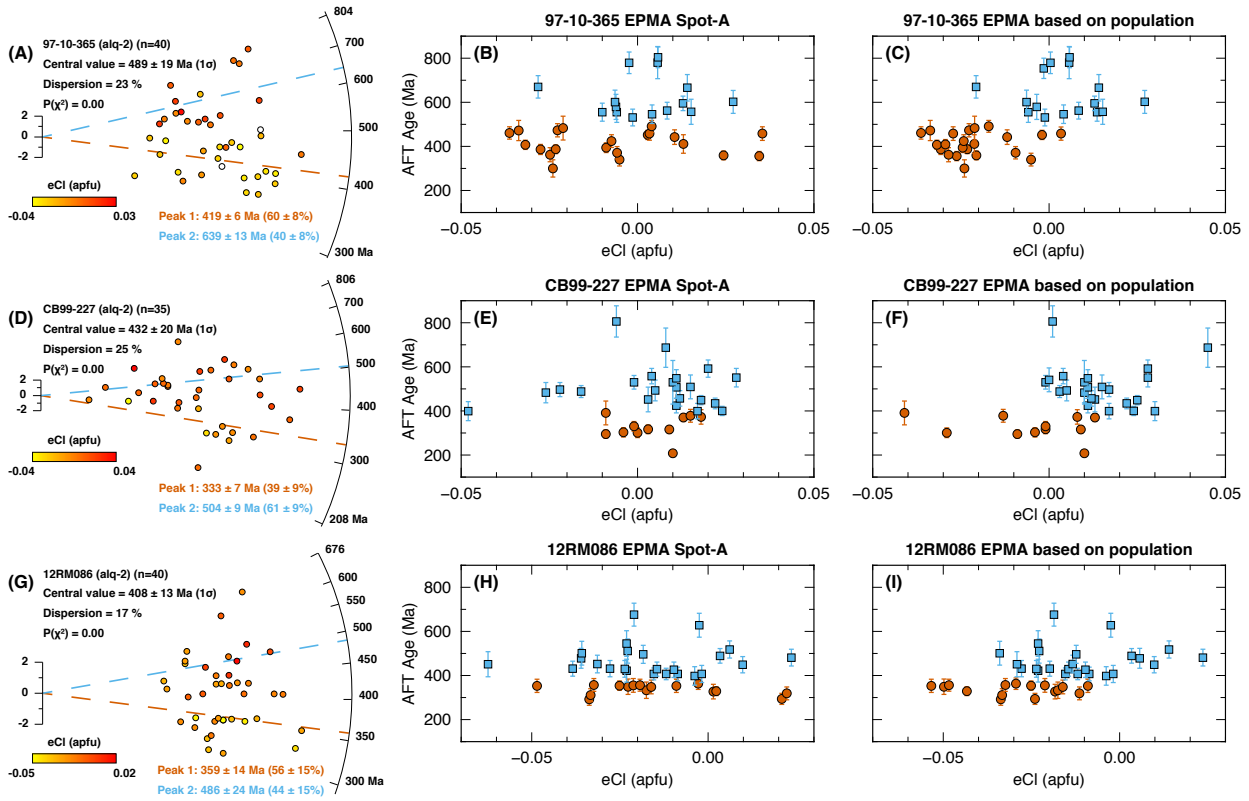

Fig. 5. (A) Radial plot of AFT ages for sample 97-10-365 aliquot-2 grains. Mixture model age peaks are dashed lines colored red or blue based on model peak age population. Points are colored by eCl value. Peak percentages are the proportion of grains in each model age group. (B) Plots of AFT age with respect to eCl for EPMA spot-A (collected near the laser ablation spot) for 97-10-365. Red circles are colored according to population-1 data and blue squares correspond to population-2 data. (C) 97-10-365 where the eCl value is either the minimum or maximum (two analyzed EPMA spots) based on kinetic population. Panels D–F descriptions are the same as above but are for sample CB99-227. Panels G–I are for sample 12RM086. Note: the radial plot points are colored by eCl values in panels C, F, and I. White points lack probe data.

acquired with respect to a conventional AFT analysis. We discuss some of the nuances involved with collecting this amount of data that are pertinent to AFT statistical treatments. We believe these are important topics to cover before discussing modelling.

The typical first step in data evaluation is examining the population statistics of the AFT apparent ages and track lengths. The χ^2 test is intended to determine if the underlying grain ages in a sample belong to a single statistical population with a common true age (Galbraith, 2005)—it is not a robust indicator of analytical data quality or a sample's suitability for modeling as is often assumed (McDannell, 2020). Failure of the χ^2 test can occur for many reasons, primarily through different annealing response between grains or by an increase in the number or precision of single-grain analyses (Vermeesch, 2017, 2019; McDannell, 2020). The latter are both typical outcomes with the LAFT method for basement rocks (for example, Ketcham and others, 2018). The χ^2 test is also sensitive to sample size, where failure is more likely with more single-grain analyses (high n). Depending on apatite yield, the external detector method (EDM) convention is to analyze $\leq$ 20 age grains, whereas LAFT analyses usually include > 20–40 grain-age analyses for bedrock samples. High age dispersion for cratonic rocks may also

be specifically related to the protracted slow cooling and differential annealing samples experienced, yielding a continuous distribution of ages rather than the typically assumed discrete age components (Vermeesch, 2019), which presents a serious challenge for interpreting the meaning of mixture-model age peaks.

LAFT age precision can also be more than double EDM precision (for example, Ansberque and others, 2021; Guibaldo and others, 2022). We have unpublished Precambrian basement samples that have LAFT single-grain age uncertainties of ~8–11% (1σ) on average, whereas EDM age uncertainties for the same samples are ~20–26% (1σ) on average. This difference in precision alone can account for the majority of LAFT χ^2 test failures. The samples presented here mostly fall into the range of ~5–10% single-grain age uncertainty. The 'improved' precision is even more influential for old Precambrian samples with high N_s track densities (and/or high U content) since the number of spontaneous tracks account for most of the AFT analytical uncertainty (Vermeesch, 2017, 2019). Precision related to N_s is apparent when examining isolated uncertainties for track counts between hypothetical apatites with N_s = 1, where $\sqrt{1}/1$ = 100% error; N_s = 100, where $\sqrt{100}/100$ = 10% error; and N_s = 400, where $\sqrt{400}/400$ = 5% error. This suggests to us that single-grain N_s counts ≤ 100 are perhaps unconsciously "ideal" from an analytical perspective and that there may be both explicit biases (for example, to obtain χ^2 passes) and implicit biases (for example, analyst confidence/experience) against routinely counting high N_s grains (for discussion, Donelick and others, 2005; Ketcham and others, 2015; O'Sullivan, 2018; McDannell, 2020).

Our samples exhibit an ambiguous or weak negative trend between single-grain ages and U ($^{238}U/^{43}Ca$ for LAFT), thought to possibly indicate "radiation-enhanced annealing" (REA) in apatite (Hendriks & Redfield, 2005) derived from Precambrian rocks (Carpéna and others, 1988; McDannell and others, 2019a). REA behavior is also present in other tectonic settings with more recent thermal overprints where low-U grains yield old ages and long track lengths and high-U grains yield young ages and short track lengths for both the EDM and LAFT methods (generally grains with low < 0.5 wt% Cl; for example, Glorie and others, 2017a,b; Fernie and others, 2018). Despite the dismissal of REA (Green and others, 2006; Green & Duddy, 2006; Kohn and others, 2009), recent laboratory experiments confirm it is a real phenomenon (Li and others, 2021)—yet Li and others concluded that REA is not an immediate concern for fission tracks in apatite because non-thermal track shortening only measurably affects zircon due to higher actinide concentrations and higher α-recoil dose compared to apatite. Currently, there is no empirical evidence to suggest AFT annealing models are inaccurate due to REA even though such kinetic models remain imperfect. A remaining question relates to the interaction of fission-track and α-recoil damage and extrapolation of lattice damage effects from the laboratory to geologic timescale. Nonetheless, these relationships remain exiguously documented and require further investigation.

It is also possible that *prima facie* REA correlations are partially a consequence of AFT ages being proportional to the ratio of track density to U concentration, or due to collecting single laser ablation spot measurements (Cogné & Gallagher, 2021). If the former was the sole source of negative correlations between AFT ages and U concentration we may expect this to be systematic for all samples, but this is not observed. There has also been

some discussion of inaccurate U measurement for low-U apatite grains, producing LAFT apparent ages that are too old (whereas the EDM yields ages that are too young for high-U grains; Seiler and others, 2013). There are, however, few if any published studies that thoroughly document this purported behavior between AFT methods. Although outside the scope of this paper we briefly discuss ongoing work related to LAFT U measurement. We carried out multi-spot tests (two spots) within minimized track count areas for Precambrian basement samples from both unpublished and published samples from McDannell and others (2019a). The AFT spot ages remained within 1σ uncertainty for different U measurements within the same track count area. Multiple U spots were combine to yield an 'averaged' multi-spot age that was within uncertainty of either individual calculated apparent age based on a single U value. This suggests that U zoning was not a problem in the samples we dated. Inaccurate or lower precision single-grain ages are expected when combining multiple U spots across large count areas and/or obviously zoned grains (Cogné & Gallagher, 2021, their fig. 1) to generate a single AFT age (Vermeesch, 2017, their fig. 2). Moreover, in a similar manner to the EDM, inspection of the etched grain surface of old apatites reveals the spatial distribution of spontaneous tracks and allows the analyst to avoid or mitigate the effects of U zonation. One source of discrepancy between LAFT and EDM apparent ages may be related to the laser ablation method accounting for the vertical U distribution, and thus U contribution of subsurface spontaneous tracks from depth in the grain (~8–10 μm)—whereas the EDM or laser rastering account for only the near-surface U (for example, Guibaldo and others, 2022). Young or U-poor apatite will remain problematic for analysis regardless of AFT method. Single-spot LAFT analyses may be overdispersed but the apparent ages likely remain accurate (Cogné & Gallagher, 2021). Put simply, both the EDM and LAFT generally produce concordant results within analytical uncertainty at accepted levels of statistical significance. We hope that ongoing research continues to inform the differences that may arise between data produced using these methods.

In spite of χ^2 failures for our samples there is no clear indication of multiple age populations due to compositional variation and the data were instead modelled as overdispersed single populations. We believe this is justified due to the aforementioned points and the fact that the LAFT method has been shown to yield greater age dispersion than the EDM, yet central tendency estimates for apparent age data still agree between both methods (Seiler and others, 2013; Vermeesch, 2017; Ketcham, 2019; Cogné and others, 2020; Cogné & Gallagher, 2021; Ansberque and others, 2021; Guibaldo and others, 2022). Our conservative interpretation is that the samples are represented by single overdispersed AFT populations due to low spread in composition and the fact that age dispersion remains generally similar when grain aliquots are combined. High LAFT age precision for old cratonic samples is the most probable source of age dispersion.

THERMAL HISTORY MODELLING

Methodology: QTQt and AFTINV software

We now discuss our thermal history modeling strategy. Inverse modelling was carried out within a Bayesian modelling framework using the QTQt v. 5.8.0 software (Gallagher, 2012). For the inversion, QTQt implements a reversible jump Markov Chain Monte Carlo (MCMC) algorithm that conducts an adaptive search of the model space while considering prior information defining the range or variability of allowable parameters such as total time-temperature range (that is, model space), allowable heating/cooling rate, kinetic annealing model uncertainty (errors on kinetic parameter; that is r_{mr0}), and more geologically based constraints such as the timing of unconformities. Parameters are randomly sampled and perturbed as individual forward models are iteratively constructed many times, yielding an ensemble of accepted t–T solutions that reproduce the observed data. The criterion for proposed model acceptance in MCMC is based on the combined prior-likelihood-proposal ratio, and simple thermal histories with fewer t–T points are generally preferred over more complex ones if the fit between the predicted and observed data is similar—hence the data play a greater role in determining the level of history complexity (rather than complexity being defined *a priori*; Gallagher, 2012; Vermeesch & Tian, 2014; Gallagher & Ketcham, 2018). Thus, if a simple history well reproduces the data, it will be preferred over a more complex one if no other prior information justifies a more complex history. This general approach is also beneficial for assessing the resolving power of low-temperature thermochronometric data with or without user-specified constraints (McDannell & Issler, 2021). An important point to reiterate is that modelling without consideration of indisputable geologic constraints is not best practice and any model output is conditional upon the input(s), therefore model predictions should always be scrutinized with respect to thermochronological observations (Gallagher, 2016).

QTQt model runs were setup with the same general prior for the thermal history: 300 ± 300 Ma and 70 ± 70°C, a modern surface temperature of 2.5 ± 2.5°C, and a maximum allowed heating/cooling rate of 3°C/My. Rate limits were imposed to prevent extreme temperature fluctuations and the acceptance of t–T paths that are unlikely for this geologic setting (the allowance of higher rates during tests did not change the form of the thermal histories). The upper model limit was not extended beyond 600 Ma because the data do not contain information relevant to the older history due to partial thermal resetting in the Phanerozoic. The multikinetic annealing model of Ketcham and others (1999) was used with the r_{mr0} kinetic parameter and track length were modelled with c-axis angle projection. Apatite composition was allowed to vary within uncertainty for the AFT data and the initial track length (L_0) was calculated based on composition. Models were run for a total of 700,000 iterations, with an initial burn-in of 200,000 iterations. The 500,000 MCMC iterations retained after burn-in were used to approximate the posterior probability distribution of model parameters.

We also carried out modeling in the AFTINV v. 6.17 software (Issler, 1996; Issler and others, 2022) that uses a model acceptance threshold based on Frequentist p-value statistics, similar to the commonly used HeFTy program (Ketcham, 2005). The primary difference between the QTQt and AFTINV, is that the latter model ensures all

accepted paths meet or exceed a certain goodness-of-fit (GOF) level based on formal statistical hypothesis tests (see Ketcham, 2005; Vermeesch & Tian, 2014; Ketcham, 2019). AFTINV uses either a nondirected Monte Carlo (MC) scheme or a Controlled Random Search algorithm (CRS; Price, 1977; Willett, 1997), or both in combination (Issler and others, 2022; McDannell and others, in press), to search parameter space for plausible thermal histories—usually 300 solutions at the 0.05 and/or 0.5 significance levels (analogous to the respective green and magenta paths in HeFTy). The AFTINV software allows various history styles to be combined to create complex thermal history scenarios with multiple phases of heating and cooling using randomly selected heating and cooling rates with temperatures calculated at fixed, user-specified time nodes (here, 5-Myr time step from 700–0 Ma). Refer to McDannell and others (2019b), McDannell & Issler (2021), and Issler and others (2022) for recent discussions of AFTINV modeling.

AFTINV models were setup similar to the QTQt models. The initial boundary conditions involve randomized selection of thermal minima within user-specified time intervals and the initial bounds were specified to require a single thermal minimum (≤ 30°C) in the Ordovician and a second thermal minimum in the middle–late Mesozoic (two randomly selected thermal peaks are also required to be ≥30°C). Maximum rates were reduced in AFTINV to 2°C/My because trial models generally exhibited rates on the order of ≤ 0.5°C/My. Furthermore, the low degree of thermal annealing experienced by our samples and the 700 My total model time make high rates prohibitive for efficiently searching t–T space. We implemented a random MC search at the 0.05 level to find 300 suitable t–T solutions that fit the AFT age and track length data at 2σ and then used the CRS algorithm to update and refine the 0.05 solution set to the 0.5 level (also 300 solutions). The CRS algorithm excels at finding multiple solution modes that fit the data (if they exist), which can be valuable for evaluating model trade-offs between data/model fit, heating-cooling rates, heating (annealing) magnitude, and minima/maxima timing. The model fits to the observed AFT age and track length distribution are calculated using the same methodology as Ketcham (2005). We mainly focus on the set of 300 CRS solutions at the 0.5 level but present the minimum objective function solution as the best model representing the entire pool. The minimum objective function (best fit) solution is defined in AFTINV as either the t–T path with the lowest combined objective function GOF for AFT age *and* the track length distribution, or the lowest maximum objective function for either the age *or* track length distribution (latter approach is used in HeFTy)—our preferred model was the one that provided the best fit to the robust track lengths, therefore the t–T path that satisfied that criterion is highlighted and discussed. We justify focus on the min. obj. function path due to the fact that the CRS algorithm optimizes the solution pool, thus overall the solutions tend to be similar in style and structure with modest differences attributed to different heating/cooling rates and locations of the thermal minima and maxima for individual paths.

QTQt Inversion Results

Models without constraints to test sensitivity.— We examined the ability of the AFT data to resolve the shield thermal history and QTQt model results are shown in fig. 6 as heat maps of t–T path density, where brighter colors

are higher relative posterior probability, that is to say, the relative frequency of the MCMC algorithm generating an accepted path through that region of t–T space. The density of paths (that is, higher relative probability) is proportional to the likelihood and is shown as the path density normalized to unity (0–1). A maximum value of 1 is equal to the upper 95^{th} percentile of path density. To be clear, the model regions with high path density generally tell us about what temperature the system was likely at in the past, but the paths in regions of higher density are not necessarily special in the sense that they are not any more likely than the other paths, because each accepted MCMC path is an equally valid draw from the posterior distribution. Subtle changes in the (log) likelihood value are more due to the transdimensional aspect of QTQt, that is, the iterative addition or subtraction of t–T points (Gallagher, 2012). The regions of high path density in the model approximate the marginal posterior probability that the "true" thermal history may have passed through that region of t–T space. It is important to keep in mind that any one point is conditional on all the other parts of the thermal history (or at least the other parts that have been integrated over all possible values of temperature).

QTQt plots show the entire accepted t–T path distribution and individual representative paths, including the maximum likelihood (ML; best fitting model shown as red curve; usually the greatest number of t–T points), maximum posterior (MP; green curve), which is the thermal history that has the maximum posterior probability, and is usually the simplest (fewest t–T points). The posterior probability combines the likelihoods and prior probabilities for each model, attempting to balance fitting the data with model complexity. The maximum mode solution (MM; gray curve) is constructed at a 1-Myr interval by running along the peak of the marginal distribution, while the Expected model is the average of the marginal distribution shown with the ± 95% credible interval (EX; black curves). The MM and EX models are not true solutions but instead summarize the accepted pool of histories. Refer to Gallagher & Ketcham (2020) for more details on individual QTQt models. The fits between the observed and predicted AFT age and track length distribution for all of the accepted paths are shown for each example (fig. 7). The accepted AFT central ages are typically at the margin of acceptability, which may be due to the lack of some high-temperature constraint to guide the inversion, or a more likely reason is that the high number of track length data have more influence on the outcome. Another secondary consideration is that QTQt does not use the central age directly during model prediction and instead transforms LAFT ages (ICPMS count and $^{238}U/^{43}Ca$ data or N_s and age ± 1σ) to external detector-equivalent data (that is, EDM; spontaneous and induced track counts; see Issler and others, 2022, for discussion). Firstly, the statistical models are different—EDM count data are based on Poissonian variables, whereas mixed ratios of Poisson and log-normally distributed variables are assumed for LA-ICPMS data (Vermeesch, 2019). There are also differences in EDM and LA-ICPMS central age estimation, where the former is the mean of the log-normal N_s/N_i ratios and the latter is typically computed as the mean of the log-normal distribution of *ages* (Vermeesch, 2018, 2019). The central ages presented in the tables are calculated from the single-grain LAFT ages and their uncertainties. The central ages calculated in QTQt slightly vary but are still reproduced within 2σ when compared to the tabulated values.

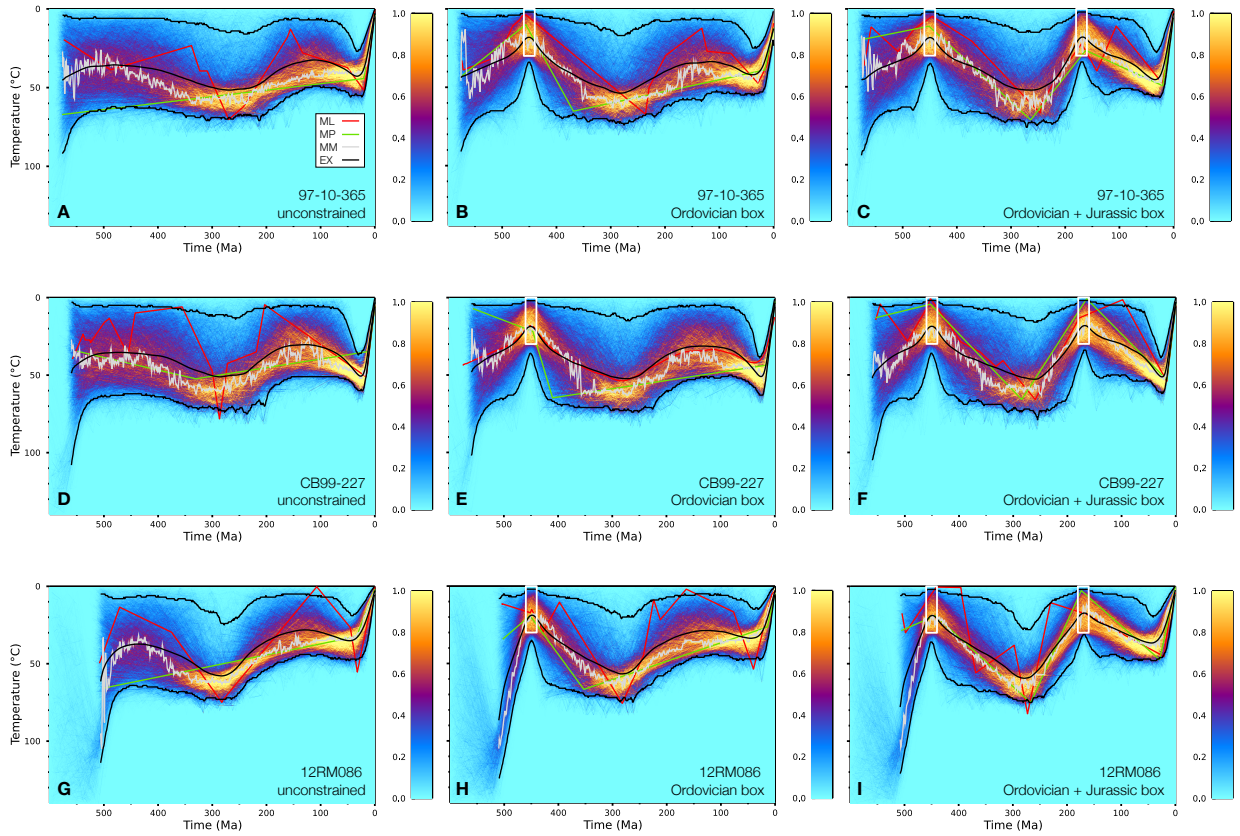

Fig. 6. QTQt time-temperature models shown as path density heat maps resolved to a pixel size of 1 My and 1 °C. Relative probability is proportional to path density, where brighter colors (or higher saturation) indicate more thermal histories pass through that region. Path density is approximately proportional to likelihood and the color scale is normalized path density (minimum value of 0 is equal to no paths, and a maximum value of 1 is equal to the upper 95^{th} percentile of path density). (A–C) model results for sample 97-10-365. (D–F) model results for sample CB99-227. (G–I) model results for sample 12RM086. Geologic constraint boxes (white) represent Ordovician and Jurassic unconformities discussed in earlier sections. A notable result is that the general features of a two-peak thermal history are visible in the unconstrained models. The robust track length datasets are better explained by two heating events and the t–T solutions independently support the regional geologic record. The other models show step-wise addition of geologic constraints and further refinement of the solutions. QTQt general prior: 300 ± 300 Ma and 70 ± 70 °C, a modern surface temperature of 2.5 ± 2.5 °C, and a maximum allowed heating/cooling rate of 3 °C/My. Each panel shows 500,000 models accepted post burn-in (200,000 iteration burn-in). ML = max. likelihood model; MP = max. posterior model; MM = max. mode model; EX = expected model. QTQt plotting script is available at: `https://github.com/kmcdannell/QTQtPlot`

We first focused on the entire stationary distribution of paths, particularly the "unconstrained" models shown in fig. 6A, D, and G. The "unconstrained" models do not include t–T constraints as prior information and here they assess the overall t–T sensitivity of the data. These examples reflect the ability of the AFT data to resolve the thermal history with the necessary level of complexity to adequately explain the data. Note that this does not mean that the true thermal history may not be more complex, but rather any additional complexity (that does not compromise fitting the data) is not actually required by the data, and so needs to be justified independently. We can see from these models that the best-fitting ML solutions require two heating peaks with a broad range in timing for both peaks due to the low magnitude of total annealing. The MP model generally shows less complexity and the data are still fit well (but not as well as the ML path) with nearly continuous cooling. Continuous cooling is unrealistic for this setting because we have independent information and prior thermochronological studies that suggest a more complex geologic history (for summary, Kohn & Gleadow, 2019). The regional geology and the best fitting t–T solutions demonstrate that two discrete thermal peaks are more likely for the central Canadian Shield.

Applied geologic constraints.— The geologic constraints were then stepwise applied to subsequent models (fig. 6B, C, E, F, H, I). The geologic information being evaluated includes two distinct times in the past that we can reasonably assume basement was at near-surface conditions (15 ± 15 °C) based on the regional information discussed previously and the "unconstrained" model results. The models imply heating occurred in the late Paleozoic and was preceded by cooler temperatures, which are constrained by the deposition of Ordovician carbonates near the AFT sample localities. The presence of thin Jurassic strata in the Moose River Basin (Norris, 1977), the *ca.* 180–170 Ma Ma kimberlite emplacement ages (Sage, 2000), and the general t–T model trends of cooler temperatures between 200–100 Ma collectively reinforce that basement was again exhumed by the Middle Jurassic. This information was sequentially added to other models as constraint boxes at: (i) 450 ± 10 Ma and (ii) 170 ± 10 Ma.

The addition of Ordovician and Jurassic constraint boxes refined the accepted t–T solutions. Model path behavior is further discussed with respect to the final models with all applied constraints to establish the general features of the thermal histories (fig. 6C, F, I). The balance between data/model fit and path complexity for the ML and MP models were considered for each AFT sample to determine simple history style behaviors. The best-fit ML model paths for samples 97-10-365, CB99-227, and 12RM086 suggest maximum Paleozoic heating to ~67 °C at 247 Ma, ~66 °C at 259 Ma, and ~82 °C at 272 Ma, respectively. The MP path for each sample exhibits maximum heating to ~71 °C at 264 Ma, ~66 °C at 284 Ma, and ~75 °C at 267 Ma, respectively. The early Cenozoic ML peak shows heating to ~40 °C at 16 Ma, ~54 °C at 16 Ma, and ~45 °C at 21 Ma, for each sample respectively. The Cenozoic MP peak shows heating to ~49 °C at 20 Ma, ~53 °C at 16 Ma, and ~47 °C at 29 Ma, respectively.

The MM model is examined here to as a generalized metric for determining the timing of maximum heating, since this model summarizes the accepted history pool using the peak of the marginal distribution, that is, the region of highest path density (the EX model is biased to lower temperatures due to smoothing and is often a poor fit to the data). The ad hoc conditional t–T criteria we applied reference the times when the modal temperature

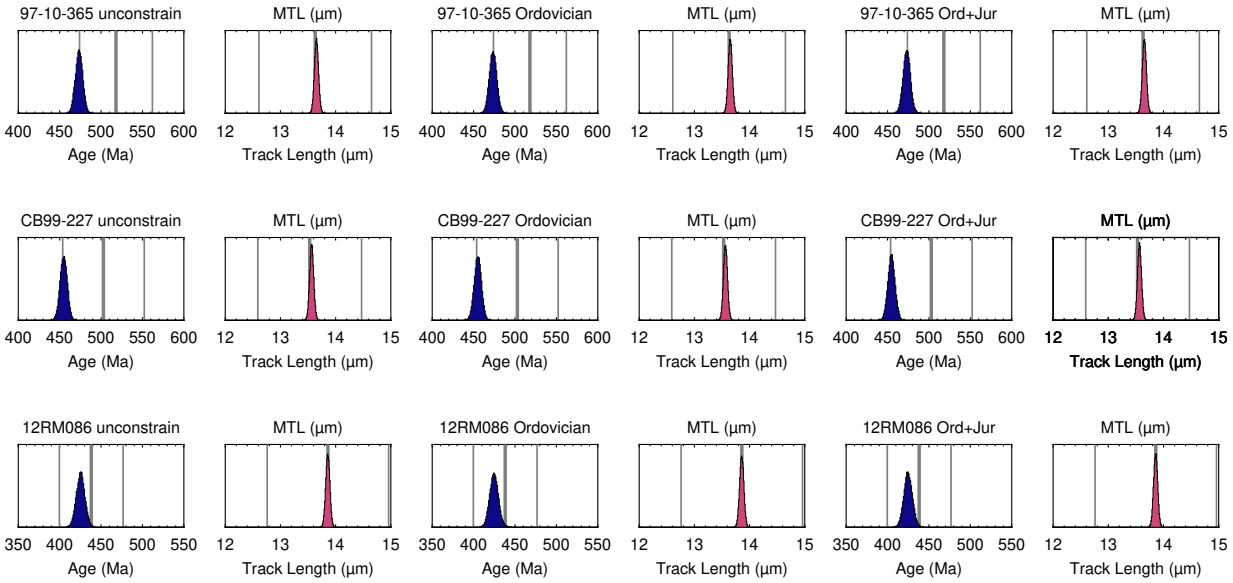

Fig. 7. The QTQt model predictions compared to the observed central AFT ages and MTLs for each model shown in fig. 6. Gray lines are the mean and uncertainty for either age (2σ) or MTL (1σ).

passed above/below ~50 °C and above/below ~35 °C for each respective thermal peak. Sample 97-10-365 displays maximum heating between *ca.* 336–223 Ma, whereas CB99-227 maximum heating occurs somewhat earlier between *ca.* 360–239 Ma, and sample 12RM086 shows maximum heating between *ca.* 356–239 Ma. The timing of the second reheating peak was estimated for sample 97-10-365 to be between *ca.* 100–17 Ma, whereas sample CB99-227 was similarly between *ca.* 94–12 Ma, and the peak for sample 12RM086 was between *ca.* 93–29 Ma. The upper 95% credible interval maximum temperature for each peak of each for the respective samples was 76 °C from 272–270 Ma and 57 °C at 25 Ma (97-10-365); 79 °C at 255 Ma and 62 °C at 26–24 Ma (CB99-227); 75 °C at 270–265 Ma and a diffuse maximum peak of ~48 °C between 95–30 Ma (12RM086). These trends suggest Paleozoic–early Mesozoic heating was of broadly similar timing and magnitude, but perhaps greater nearer to the Moose River Basin, whereas the late thermal peak was consistently early Miocene (latest Oligocene?, but as early as Cretaceous) and similar in magnitude across the Hudson Platform.

Conditional probabilities.— Determining conditional probabilities is a practical way to evaluate model correlations and provide an additional test of the level of model non-uniqueness and data sensitivity in a Bayesian QTQt model (for example, Fox & Carter, 2020). Do some accepted paths in the posterior distribution contain distinct thermal history characteristics? The parameters (time and temperature) of the inverse problem are highly correlated—any change in temperature at one point in time within a specific thermal history path can be compensated by an opposing change in temperature at another point in time (Willett, 1997)—thus the (marginal) probabilities are dependent on all aspects of a candidate thermal history. The relative probability is a way to visualize the likelihood that the true thermal history passes through a certain region of t–T space—which can be achieved by either all histories sharing some similar t–T trend, or by structurally different paths all passing through the same

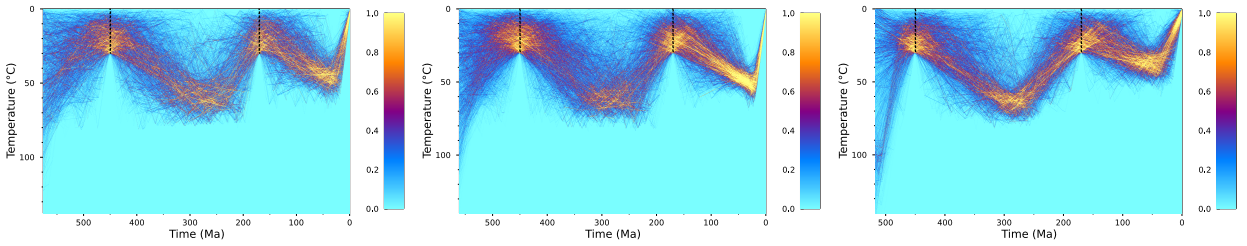

(a) sample 97-10-365 (b) sample CB99-227 (c) sample 12RM086

Fig. 8. Conditional probabilities for the 'unconstrained' QTQt models given that the AFT samples cooled to near-surface temperatures (0–30 °C) at 450 Ma and 170 Ma. Histories were filtered by imposing time-temperature "gates" (black dashed lines) such that only those histories that met the specified conditions were retained. All other QTQt model options are the same as those discussed previously. Note that these are not new models but are those shown in fig. 6; panels A, D, and G, respectively.

part of time-temperature space. For models without imposed constraints, the posterior model distribution may contain paths with a varying, finite number of t–T points and different solution modes (that is, thermal history styles) that overlap with one another and may impart the sense that certain features of the history are more probable or are inconsistent with some known geologic constraint, when in fact that feature is reproduced by a subset of histories and is simply obscured by other solutions.

Here we show an example of applying conditional probability tests (fig. 8) to the 'unconstrained' QTQt models for each AFT sample in fig. 6 (panels A, D, and G). This can be considered a retroactive or *a posteriori* probability "filtering" of the entire accepted thermal history pool by retaining only the paths that, in this case, are at near-surface temperatures (0–30 °C) at both 450 Ma and 170 Ma (discarding all other paths). These conditional models clearly exhibit the same thermal history features as those in fig. 6C, F, and I with *a priori* enforced geologic conditions. The older Precambrian history is poorly resolved without other medium- to high-temperature thermochronometers (in the absence of assuming certain geologic conditions in the late Neoproterozoic). The pre-450 Ma history demonstrates that for all samples the AFT data can be explained by some combination of cooling from temperatures near 100 °C or by residence at low temperatures due to thermal resetting. A nearby Hudson Platform sample locality (see fig. 2) reinforces this notion (McDannell & Keller, 2022). The QTQt model shown in McDannell & Keller (2022) incorporated the zircon (U–Th)/He, AFT, and apatite (U–Th)/He thermochronometers to yield a deep-time thermal history illustrating rapid cooling and exhumation during the Cryogenian followed by cooler conditions (< 50 °C) prior to Paleozoic heating, which was interpreted as the basement being located near the surface between *ca.* 635–475 Ma.

AFTINV Inversion Results

The QTQt results exhibit general t–T trends that are useful for determining the surface history of the Hudson Platform. We used the QTQt results and the regional geology to infer a history style that involves initial random cooling followed by two random heating-cooling cycles. The primary goal of AFTINV modeling was to compare model results generated with similar boundary conditions as QTQt but with a different statistical approach for

thermal history acceptance. Since our samples are far from preserved Mesozoic rocks and there are more temporal and spatial uncertainties related to the late Paleozoic–Mesozoic Hudson Platform surface evolution, we investigated different thermal minima scenarios within the Paleozoic and Mesozoic intervals in AFTINV (that is, timing based on QTQt model results and the regional geology). This is a useful exercise because cratonic nonconformities can be misleading. Unconformities are features that potentially elide multiple periods of erosion and sedimentation—yet we typically have information only constraining the upper age limit of the depositional event that terminated the unconformity. Therefore our constraint for basement being near the surface at 450 Ma or 170 Ma may actually represent a fraction of a much longer period of time when the Precambrian basement was near the surface. The Ordovician nonconformity also does not preclude earlier basement exposure and the nearby presence of the Cambrian (*ca.* 505 Ma) Deadwood Fm. in the Williston Basin (for example, Burrus and others, 1996) and the *ca.* 530 Ma Mt. Simon Sandstone in the Michigan Basin (for example, Catacosinos and others, 1990) could imply regional exposure and localized shallow burial and erosion prior to the Ordovician. We further evaluated the Paleozoic and Mesozoic thermal minima to allow the model to query between 470–450 Ma and 200–120 Ma, which is generally based on the Hudson Platform geology and the QTQt results. Sample 12RM086 required slightly different boundary conditions to achieve timely model convergence. A maximum of 5 °C/My cooling was allowed for the initial pre-450 Ma history (justified by QTQt results), due to the younger central age and less retentive average kinetics than the other two samples. In AFTINV the only requirement for the thermal minimum is that a single, randomly chosen 5 Myr time step is ≤ 30 °C within each search interval, however this does not prevent other (contiguous) steps from being at similarly low temperatures in the model.

Sample 97-10-365.— The AFTINV results yielded temperatures for the first thermal peak between 69–81 °C, with a weighted mean temperature of 75 ± 2 °C. The timing of the peak is between 210 Ma and 400 Ma, with a weighted mean time of 311 ± 29 Ma (2σ). The second thermal peak reached temperatures between 51–66 °C, with a weighted mean temperature of 58 ± 3 °C. The timing of the second peak is between 25 Ma and 115 Ma, with a weighted mean of 47 ± 27 Ma. The values reported here incorporate the solutions at both the 0.05 and 0.5 levels of significance (table 4). It is also important to keep in mind that the time step used in AFTINV was 5 Myr, therefore we lack temporal resolution below that value for individual times (i.e., minima or maxima).

Sample CB99-227.— The AFTINV results yielded temperatures for the first thermal peak between 72–83 °C, with a weighted mean temperature of 75 ± 2 °C. The timing of the peak is between 215 Ma and 415 Ma, with a weighted mean time of 319 ± 40 Ma (2σ). The second thermal peak reached temperatures between 52–72 °C, with a weighted mean temperature of 62 ± 3 °C. The timing of the second peak is between 25 Ma and 115 Ma, with a weighted mean of 49 ± 23 Ma.

Sample 12RM086.— The AFTINV results yielded temperatures for the first thermal peak between 68–80 °C, with a weighted mean temperature of 72 ± 2 °C. The timing of the peak is between 225 Ma and 385 Ma, with a weighted mean time of 314 ± 26 Ma (2σ). The second thermal peak reached temperatures between 43–63 °C, with

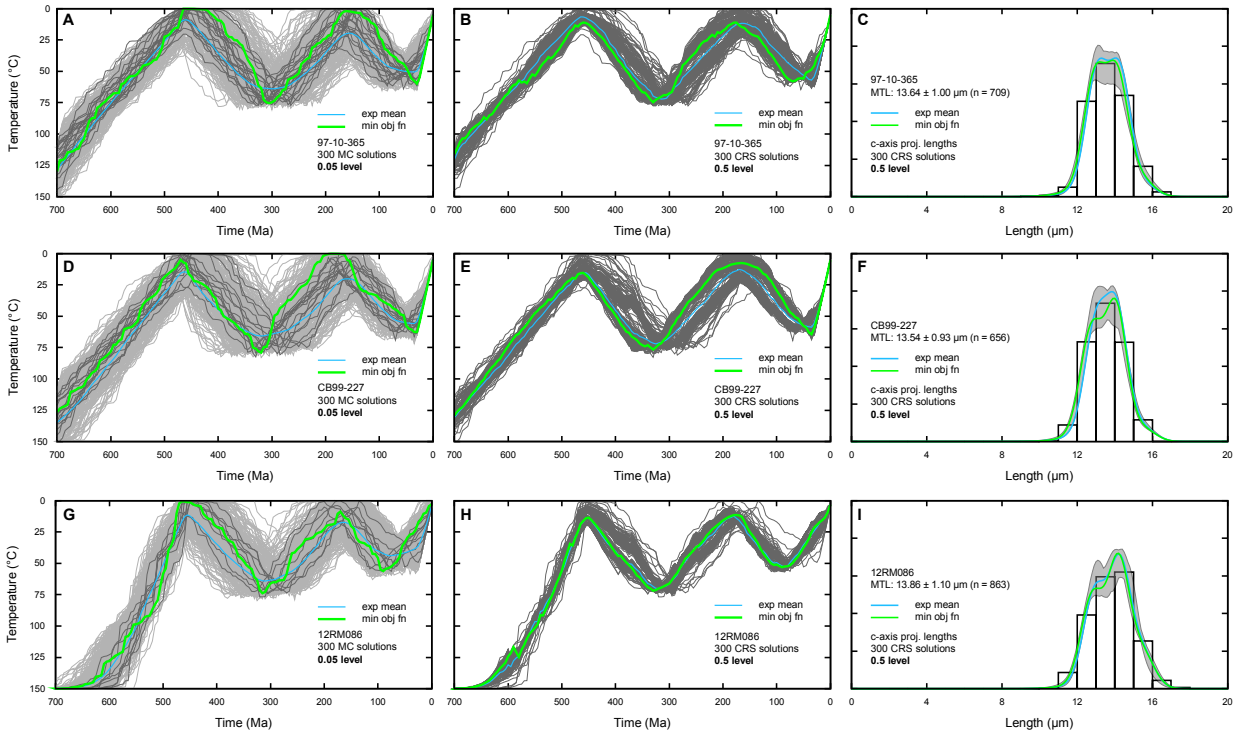

Fig. 9. AFTINV inverse model results for the Hudson Platform samples. Panels A, D, and G show 300 acceptable random Monte Carlo solutions at the 0.05 significance level (light gray t–T paths). Some 0.5 significance level solutions were randomly found during the initial Monte Carlo search (dark gray paths) and were retained in the solution pool. The 0.05 random MC solution set for each AFT sample was then updated by the CRS algorithm to the 0.5 significance level. Panels B, E, and H show 300 acceptable solutions at the 0.5 significance level (dark gray t–T paths) obtained using the CRS algorithm. The exponential mean (exp mean; blue line) solution and the best-fit minimum objective function (min obj fn; green line) solution are also shown for the MC and CRS paths. Panels C, F, and I show the better 0.5 level fits to the track length distributions as a gray envelope for all solutions and the best fit and mean are highlighted in green and blue. The 0.5 level goodness-of-fit values for the track lengths are 0.98, 0.88, and 0.93 for samples 97-10-365, CB99-227, and 12RM086, respectively. Refer to table 4 for tabulated information on the GOFs for AFT age and length for each model. Figure 10 summarizes the thermal peak timing and magnitude for the 0.05 and 0.5 fit levels. Note that the time and magnitude of heating between the QTQt and AFTINV results are similar, yet the QTQt results more closely resemble the 0.05 solution set from AFTINV.

a weighted mean temperature of 53 ± 3 °C. The timing of the second peak is between 25 Ma and 115 Ma, with a weighted mean of 82 ± 14 Ma.

DISCUSSION

Burial and Erosion History Interpretations

Nearly identical Phanerozoic thermal histories are recovered for all of the samples in QTQt and the models independently corroborate the known cratonic geology by requiring two reheating events that we interpret as sedimentary burial (fig. 6). It is worth noting that the same priors were used for the three samples (that are in close proximity to one another), so the similarity in the model results demonstrates that a similar history can satisfy all of the data. The thermal histories suggest poorly resolved surface conditions in the late Precambrian to early Paleozoic (fig. 6) and also indirectly require periods at lower temperatures in the middle Mesozoic. The low temperatures are necessary to form a population of tracks that are then shortened by reheating to produce

Table 4. AFTINV v. 6.17 model results for single kinetic population Hudson Platform AFT samples

	97-10-365		**CB99-227**		**12RM086**	
	0.05 LEVEL	**0.5 LEVEL**	**0.05 LEVEL**	**0.5 LEVEL**	**0.05 LEVEL**	**0.5 LEVEL**
search algorithm	MC	CRS	MC	CRS	MC	CRS
model results	300 solutions	300 solutions	300 solutions	300 solutions	300 solutions	300 solutions
	BEST MODEL FITS*		**BEST MODEL FITS**		**BEST MODEL FITS**	
AFT Age (± 2σ)	512 ± 36 Ma	512 ± 36 Ma	487 ± 44 Ma	487 ± 44 Ma	433 ± 24 Ma	433 ± 24 Ma
Model AFT Age	505.3 Ma	511.4 Ma	490.6 Ma	491.4 Ma	429.4 Ma	433.8 Ma
Age GOF	0.70	0.96	0.85	0.82	0.75	0.97
Length GOF	0.93	0.98	0.84	0.88	0.74	0.93
Retention Age	653 Ma	673 Ma	648 Ma	650 Ma	538 Ma	545 Ma
	THERMAL PEAK 1		**THERMAL PEAK 1**		**THERMAL PEAK 1**	
temp. minimum	69 °C	71 °C	72 °C	72 °C	68 °C	69 °C
temp. maximum	81 °C	77 °C	83 °C	82 °C	80 °C	77 °C
mean ± 2σ	75 ± 4 °C	75 ± 2 °C	77 ± 4 °C	75 ± 2 °C	73 ± 4 °C	72 ± 2 °C
time minimum	210 Ma	250 Ma	215 Ma	235 Ma	225 Ma	255 Ma
time maximum	400 Ma	355 Ma	415 Ma	370 Ma	385 Ma	345 Ma
mean ± 2σ	298 ± 72 Ma	313 ± 32 Ma	308 ± 80 Ma	322 ± 46 Ma	302 ± 64 Ma	316 ± 28 Ma
	THERMAL PEAK 2		**THERMAL PEAK 2**		**THERMAL PEAK 2**	
temp. minimum	51 °C	51 °C	52 °C	57 °C	43 °C	46 °C
temp. maximum	66 °C	64 °C	72 °C	69 °C	63 °C	57 °C
mean ± 2σ	59 ± 6 °C	58 ± 4 °C	62 ± 4 °C	62 ± 4 °C	53 ± 6 °C	53 ± 4 °C
time minimum	25 Ma	30 Ma	25 Ma	30 Ma	25 Ma	25 Ma
time maximum	115 Ma	90 Ma	115 Ma	75 Ma	115 Ma	115 Ma
mean ± 2σ	55 ± 48 Ma	44 ± 32 Ma	52 ± 40 Ma	47 ± 28 Ma	66 ± 54 Ma	83 ± 14 Ma
	BEST FIT PATH MINIMA**		**BEST FIT PATH MINIMA**		**BEST FIT PATH MINIMA**	
min time 1	465 Ma	460 Ma	470 Ma	460 Ma	465 Ma	450 Ma
min time 2	160 Ma	175 Ma	190 Ma	170 Ma	170 Ma	175 Ma
	INFORMATION		**INFORMATION**		**INFORMATION**	
modeled r_{mr0}	0.840 (0.0 apfu eCl)		0.837 (0.01 apfu eCl)		0.848 (-0.025 apfu eCl)	
min. obj. sol.	lowest combined obj. fn.		lowest max. obj. fn.		lowest combined obj. fn.	
c-axis MTL	13.64 ± 1.00 μm		13.54 ± 0.93 μm		13.86 ± 1.10 μm	
lengths (n)	709		656		863	

*Model fits are shown only for the minimum objective function solution. Information about the thermal peaks is for all 300 solutions at the corresponding significance level. Retention age is the hypothetical oldest preserved fission track and approximates the upper limit of t–T sensitivity. Initial cooling (timing) prior to the first thermal minimum should not be fully interpreted since samples are partially reset and cooling is a function of the model rates and random thermal minimum selection under the prescribed model conditions.

**Minima were randomly selected between 470 Ma and 450 Ma (followed by thermal peak 1) and 200 Ma and 120 Ma (followed by thermal peak 2) and are given for the single 5 Myr time step that is at the lowest temperature in the model run. These times are approximations since there are sometimes multiple consecutive time steps at similar temperatures. Model time step is 5 Myr but sub-step time for fission track generation is 2.5 Myr.

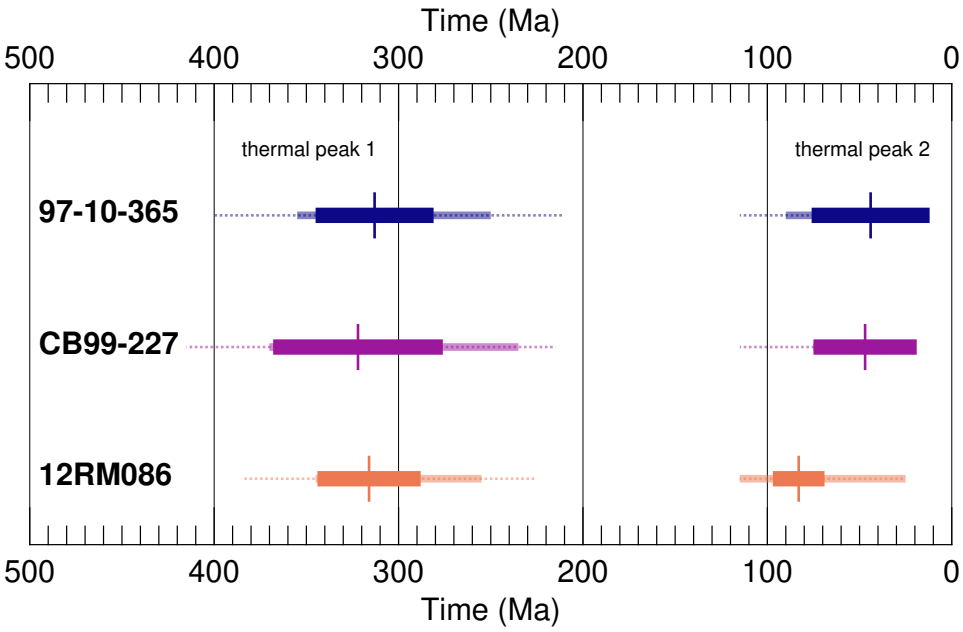

Fig. 10. Thermal episode summary for the AFTINV inverse thermal history models exhibiting two thermal peaks. Dotted line shows the minimum-maximum time range at the 0.05 significance level for each thermal peak for each sample. Thick transparent line represents the minimum-maximum time range at the 0.5 significance level. The vertical bar and opaque heavy lines show the mean ± 2σ time for each thermal peak at the 0.5 level. Refer to table 4 for tabulated information.

the observed lengths—without this, a certain component of lengths cannot be generated that are needed to fit the observations. The inverse models best resolve a broad thermal peak between approximately latest Devonian to Triassic (*ca.* 360 to 240 Ma) for all samples that is consistent for all simulations (fig. 6; albeit more resolved in panels C and F). The timing of maximum temperature is poorly constrained due to the low degree of thermal annealing within the PAZ for these apatites and also partially reflects the trade-off between t–T path inflections (i.e., uncertainty on the times at hotter vs. cooler temperatures; fig. 6A–B, D–E) and the allowable heating-cooling rates imposed on the solutions. Step-wise addition of the Ordovician and Jurassic constraint boxes (fig. 6B–C and E–F) refine the overall history results and the requirement of two heating events by the AFT data suggest maximum heating to ~65–75 °C occurred in the Devonian, or possibly in the latest Paleozoic, in broad agreement with the preserved geology.

We interpret the heating in our models as burial by Phanerozoic sedimentary rocks and the thermal histories are in close agreement with other thermochronology studies across the southern shield near the Hudson Bay and Williston Basins (for example, Crowley & Kuhlman, 1988; Crowley, 1991; Kohn and others, 1995; Osadetz and others, 2002; Kohn and others, 2005; Feinstein and others, 2009). The QTQt results suggest maximum burial heating likely occurred sometime between the late Devonian and early–middle Triassic, with a second event in the late Cretaceous to early Miocene across the Hudson Bay region. The AFTINV results provide a refinement of these burial estimates (table 4; figs. 9 and 10). The earliest peak burial times are consistent with the age of the preserved upper Devonian section (Pinet and others, 2013; Lavoie and others, 2015; Armstrong and others, 2018), whereas the existence of

Carboniferous (for example, Tillement and others, 1976) and Permo-Triassic strata that were subsequently eroded cannot be ruled out. The Michigan and Williston basins contain a few hundred meters of Pennsylvanian and Jurassic strata (Sloss, 1963; Catacosinos and others, 1990; Burrus and others, 1996; Burgess, 2019), which perhaps suggests a common Paleozoic history for interior North America (for example, Beaumont and others, 1987; Sanford, 1987; Burgess and others, 1997; Patchett and others, 1999). However, central Canadian Shield burial during the Carboniferous and the presence of rocks of that age in the Hudson Bay Basin are debated. Possible explanations for these features in our inversions are that: (i) Pennsylvanian strata are actually preserved in the Hudson Bay Basin and Tillement and others (1976) were correct, or (ii) that presumably thin Carboniferous rocks were deposited but were then eroded as a result of lower preservational potential near the modern basin margin (also Hudson Bay is shallower in general compared to the other deeper intracratonic basins), or (iii) Carboniferous strata were not deposited in the Hudson Bay region and the late Paleozoic heating event in our models is highly uncertain. While there is uncertainty in the peak timing (point iii), the thermal peak is consistent for three different AFT models, whereas the preserved geology cannot be relied upon to provide a faithful record of sedimentation. The AFT inversions and the findings of Tillement and others (1976) support minor Carboniferous burial of the central shield.

The Mesozoic-Cenozoic history is characterized by inferred burial followed by subsequent erosion until present day, with the final cooling event beginning as late as Oligocene–Miocene time. The White River Group (< 38 Ma in age) in the Williston Basin provides tentative geological support for this, as it records the last burial event during the Paleogene, which was followed by Miocene erosion (Burrus and others, 1996). While speculative, it is possible that some of the latest model cooling could be attributed to climatic cooling since the timing approximately aligns with climate change and the growth of the Antarctic ice sheet, including ephemeral northern hemisphere Oligocene-Miocene continental glaciation (Eldrett and others, 2007; DeConto and others, 2008; Hyeong and others, 2014; Tripati & Darby, 2018). Our thermal history models further imply that burial extended across the currently exposed basement of the Canadian Shield, that the Hudson Bay sedimentary succession is an erosional remnant (for example, Pinet and others, 2013; McDannell and others, in press), and that the Hudson Bay and Williston basins were probably intermittently connected (for example Sanford, 1987; Norris, 1993; White and others, 2000).

We applied a range of feasible Phanerozoic paleosurface temperatures (Mills and others, 2019; Scotese and others, 2021): 15–20 °C for the Paleozoic and 20–30 °C for the Cretaceous. Paleogeothermal gradient estimates for the Paleozoic (40–50 °C/km) and Mesozoic (20–25 °C/km) were based on the nearby Underground Research Laboratory (URL) borehole thermal history reconstruction in SW Manitoba (Feinstein and others, 2009). We set a minimum thermal gradient of 30°C/km for the Paleozoic since the estimate from Feinstein and others (2009) is quite high and may have been brief or a local anomaly. The AFTINV minimum and maximum temperatures for each model thermal peak at the 0.5 significance level in table 4 indicate mean burial depths of ~1.5 ± 0.7 km (97-10-365; 2σ), ~1.6 ± 0.7 km (CB99-227), and ~1.3 ± 0.6 km (12RM086) in the Paleozoic. The late Mesozoic-early Tertiary thermal peaks translate to burial of ~1.5 ± 0.9 km (2σ), ~1.7 ± 0.9 km, and ~1.2 ± 0.8 km for each respective sample.

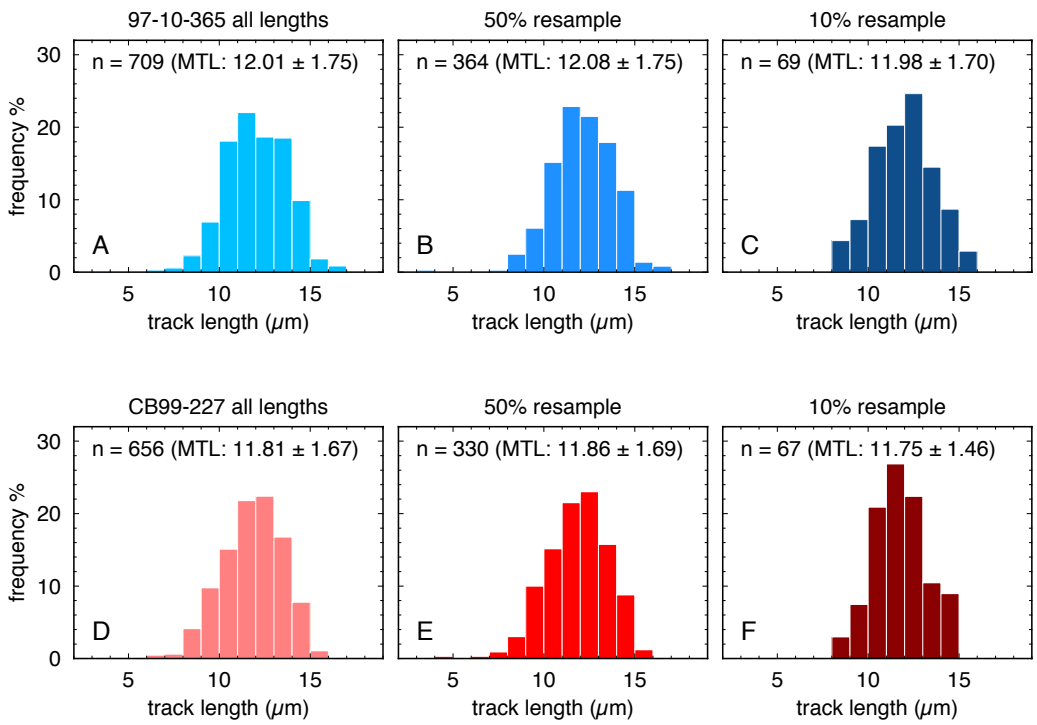

Fig. 11. Conventional unprojected track length distributions for two AFT samples as histograms with 1 μm bins. Track lengths are displayed as they were originally measured but were modelled using their corresponding *c*-axis angles. (A) all 709 track lengths combined from both sample aliquots of 97-10-365 with a conventional mean track length of 12.01 ± 1.75 μm and *c*-axis projected mean length of 13.63 ± 1.02 μm. (B) random 50% downsampling or resampling of the total number of lengths in panel A. (C) random 10% resampling of the total lengths in panel A. (D–F) Sample CB99-227; the same as panels A–C with a conventional mean track length of 11.81 ± 1.67 μm and *c*-axis projected mean length of 13.53 ± 0.94 μm. All resampled distributions in panels B–C and E–F are similar in form to the ones in A and D, respectively. MTL = mean track length.

These estimates tentatively suggest a thinning of burial cover from the NW to the SE towards the Transcontinental arch (see fig. 3) during both time periods.

Comments on Track Length Data Collection for Deep-Time Applications

The principle source of uncertainty in fission-track length data is the discrete number of finite lengths collected rather than measurement error (Willett, 1997). Inadequate characterization of length distributions may affect our ability to recover thermal history information. While this is not conceptually novel (Ketcham and others, 2009)—what constitutes a robust track length dataset and if those data can independently support geologic observations has gone mostly unrecognized. The results of our modelling emphasize that the accepted norm of collecting up to 100 track lengths (for example, Rahn & Seward, 2000) is possibly too low for many deep-time modelling applications. We point out that this is more of an issue for situations that lack suitable guiding constraints for inversions, or cases where individuals do not prefer to make numerous *a priori* assumptions about a geologic history. This may not be a concern for endmember approaches that purposefully minimize the degrees of freedom in thermal history models (for example, Green & Duddy, 2012; Green and others, 2022).

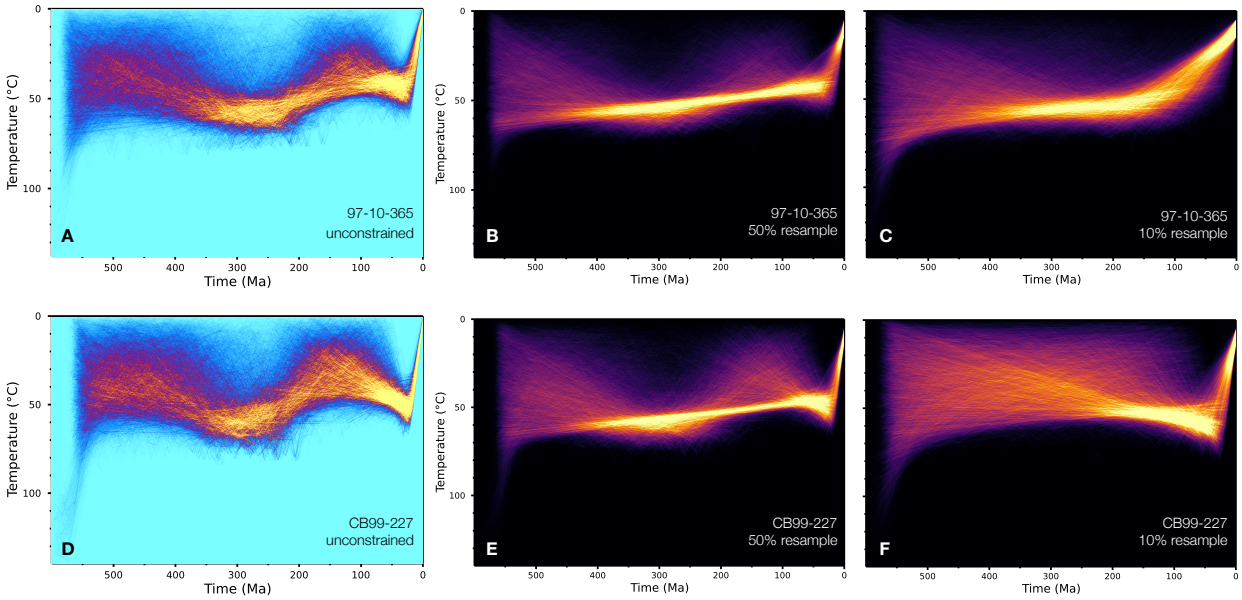

Fig. 12. QTQt time-temperature simulations shown as path density heat maps. Panels A and D are the 'unconstrained' models without t–T constraint boxes shown in fig. 6. Models in the other panels are shown with a different color ramp to distinguish from those models. (A) model results for the total 97-10-365 length dataset (B) model results for the 50% (n = 364) randomly resampled track lengths and (C) 10% (n = 69) resampled tracks for sample 97-10-365. (D) model results for the total CB99-227 length data set. (E) model results for the 50% (n = 330) randomly resampled track lengths and (C) 10% (n = 67) resampled tracks for sample CB99-227. The two-peak history is not well resolved below ~250–300 track lengths (note: longer inversion burn-in may potentially help resolve the two thermal peaks (vs. more linear history) in panels B and E).

In detail, many different thermal histories can satisfy a given track length distribution. However, even if the distribution looks similar between an example with many tracks and fewer tracks, the possibility to resolve multiple heating-cooling events in a history is reduced in the latter case. While the mean track length is a useful summary statistic, it is the width and shape of the track length distribution that are critical for modelling (Crowley, 1985; Gleadow and others, 1986b). The main body of the distribution needs to be well defined with many tracks, but the tails of the true distribution also need to be well represented. Namely, any shorter lengths that provide key temperature information must be included, which will typically require more measurements because they have a lower probability both of being observed and measured accurately (Laslett and others, 1982). The c-axis angle projection of track lengths also plays a role by reducing length dispersion due to track orientation (Donelick and others, 1999). This yields a better defined length distribution—thereby taking advantage of the extra information provided by the annealing dependence on track orientation (Ketcham and others, 2009; Ketcham, 2019). If the distribution shape is well characterized then the thermal model can deconvolve the mixed length components generated by the different heating-cooling cycles. Attempts to understand this in the past may have been hindered by a lack of collected data. We consider how the number of confined track lengths affects our ability to reconstruct the thermal history in QTQt and examine whether a typical AFT analysis with 50–100 track lengths contains enough information for cratonic thermal history reconstruction without imposing numerous model assumptions within a Bayesian framework.

Track Length Resampling: Sensitivity Tests

Our simulations clearly show that our AFT super-samples have enough track lengths to require two thermal events (i.e., without requiring t–T boxes) during the Phanerozoic. The inferred complexity of a thermal history (fig. 1) can be partially related to the number of track lengths that are collected by the analyst and how well those lengths define the real distribution. To further explore this, we took the entire length datasets for two examples and randomly downsampled them using a simple Monte Carlo method, retaining ~50% and ~10% of the tracks in the original length distributions while maintaining a stable mean length within uncertainty (fig. 11). This was done to determine how well we resolve the two thermal peaks in the full model t–T history from fig. 6A and D with a reduced number of length measurements. This essentially simulates what a real AFT analysis would be like if fewer length measurements were collected. Each resampled distribution was modelled in QTQt, while keeping the AFT age information fixed to assess how resampling of the total number of track lengths affected t–T resolution. The results shown in fig. 12 indicate that there is an inadequate number of track lengths in a typical AFT analysis (≤ 100 lengths) to fully resolve a complex cratonic thermal history involving moderate annealing without applying interpretation-based constraints. This was discussed conceptually as a intuitive result in McDannell & Issler (2021) and McDannell and others, (in press). The thermal histories become more linear with less structure and the resolution of two thermal peaks is progressively reduced for ~300–350 lengths (fig. 12B–E) and disappears with < 100 tracks (fig. 12C–F). Thus fewer track lengths (and no other independent constraints) create a situation where simpler histories can reproduce the AFT data. Conversely, reduced t–T sensitivity also implies that the data would be less sensitive to certain applied constraint boxes, some of which may be incorrect, in cases with fewer thermochronometric data (track lengths being the most important for AFT). One could argue that collecting more track lengths assumes that our AFT kinetic annealing models are well determined, even though uncertainty in such models remains a reality. However, we would argue that collecting more track lengths resulted in thermal histories that independently agree with the known geologic record for the Hudson Platform. This finding suggests that collection of up to > 500 track lengths does not result in 'overfitting' the data and that the modern AFT kinetic annealing model(s) in use (Ketcham and others, 1999, 2007) are reasonably calibrated and remain the best empirically constrained of the available thermochronometric methods. It is, however, apparent that some published QTQt models with ≤ 100 measured AFT lengths (without imposed constraints or limited supplemental (U–Th)/He dates) lack sensitivity and are a primary reason that simple, linear cooling thermal histories are recovered for models spanning 100s of Myr.

Ultimately, each problem is unique and analyses should be tailored to optimize the amount of information available for modelling since we know that a standardized approach may not yield sufficient data to clearly resolve significant thermal events. If a sample has undergone more recent total annealing and resetting, the collection of additional track lengths will provide (minimal) t–T information in proportion to the total amount of geologic time being reconstructed and the timing of thermal resetting. We recommend that 250–300 confined track lengths (with

c-axis angles) may be considered an effective minimum suitable for thermal history inversion in cratonic settings for rocks that contain a single kinetic population and have experienced low-to-moderate thermal annealing. This simple change in analytical protocol may improve thermal history recovery using Bayesian methods and lend more credence to geologic interpretations in slowly cooled continental interiors.

CONCLUSIONS

Studies of cratons have shown that they are typically characterized by thermal histories involving low to moderate degrees of thermal annealing from episodic sedimentary burial (see Kohn & Gleadow, 2019). Apatite fission-track dating has traditionally been a preferred method for constraining aspects of these complex burial and erosion events. However due to the near absence of physical geologic constraints, detailed thermal history reconstruction is often difficult. This commonly results in a modelling approach that incorporates interpretive assumptions about a geologic history that may be inappropriate or at least difficult to validate independently. We discussed different strategies for inverse modelling applied to new apatite fission-track data from the central Canadian Shield that included many more confined track-length measurements than a typical fission-track analysis. Inversions of those data yielded results that are consistent with the regional shield geology without necessarily requiring the imposition of many t–T "exploration boxes". Subsequently, consideration of known geologic constraints with different inversion approaches allowed an assessment of the impact of constraints relative to models that did not apply a presupposed interpretive geological model. Within the AFT modelling framework outlined here, we recommend that > 250 track lengths be collected when possible to provide adequate and robust time-temperature information for cratonic history inversions using Bayesian methods and for the wider adoption of recursive modelling practices in situations where geological control is a limiting factor in thermal history reconstruction. Inverse thermal histories for Hudson Platform AFT data suggest peak sedimentary burial during the late Paleozoic to earliest Mesozoic and later during the latest Mesozoic to mid-Cenozoic. Overall burial average estimates are 1.4 ± 0.7 km (2σ) for the Paleozoic and 1.5 ± 0.9 km for the late Mesozoic. These average estimates imply ~3 km of total Phanerozoic erosion for currently exposed locations with a negligible contribution to the erosional budget from the crystalline basement. This gives credence to the concept that the Canadian Shield is a regenerative geomorphic feature that was first formed in the Precambrian but has undergone repeated exposure throughout Earth history.

AUTHOR CONTRIBUTIONS

CRediT author statement. *K. McDannell*: Conceptualization, Investigation, Methodology, Formal analysis, Visualization, Funding acquisition, Writing - original draft; *P. O'Sullivan*: Formal analysis, Methodology, Resources; *K. Gallagher*: Methodology, Validation, Writing - Review & Editing; *S. Boroughs*: Formal analysis, Methodology, Resources

ACKNOWLEDGMENTS

The Government of Canada Geomapping for Energy and Minerals Program (GEM-2) supported K.T.M. at the Geological Survey of Canada, Calgary from 2017–2020 during data collection. This work was specifically supported with funds to K.T.M.

through the GEM-2 geological synthesis. Thanks to Michel Plouffé (GSC Ottawa) for GEM program coordination. Nicolas Pinet (GSC Québec) and Christian Böhm (Manitoba Geological Survey) are thanked for correspondence and providing rock samples for analyses. C.B. Keller is thanked for assistance with Julia code.

SUPPLEMENTARY DATA

LAFT ages/lengths and electron microprobe data are available from the Open Science Framework (OSF) repository: `https://osf.io/73u8j/`

REFERENCES

Ahern, J. L., & Mrkvicka, S. R., 1984, A mechanical and thermal model for the evolution of the Williston Basin, Tectonics, v. 3, n. 1, p. 79–102, https://doi.org/10.1029/TC003i001p00079.

Anderson, S., Böhm, C., & Syme, E., 2010, Far North Geomapping Initiative: bedrock geological investigations in the Seal River region, northeastern Manitoba (parts of NTS 54L, M, 64I, P), In Report of Activities 2010, p. 6–22. Manitoba Innovation, Energy and Mines, Manitoba Geological Survey.

Ansberque, C., Chew, D. M., & Drost, K., 2021, Apatite fission-track dating by LA-Q-ICP-MS imaging, Chemical Geology, v. 560, p. 119977, https://doi.org/10.1016/j.chemgeo.2020.119977.

Armstrong, D. K., Nicolas, M. P. B., Hahn, K. E., & Lavoie, D., 2018, Stratigraphic synthesis of the Hudson Platform in Manitoba, Ontario, and Nunavut: Ordovician-Silurian, Tech. rep., Geological Survey of Canada, Open File 8378, https://doi.org/10.4095/308418.

Ault, A. K., Flowers, R. M., & Bowring, S. A., 2009, Phanerozoic burial and unroofing history of the western Slave craton and Wopmay orogen from apatite (U-Th)/He thermochronometry, Earth and Planetary Science Letters, v. 284, n. 1-2, p. 1–11, https://doi.org/10.1016/j.epsl.2009.02.035.

Barbarand, J., Carter, A., Wood, I., & Hurford, T., 2003, Compositional and structural control of fission-track annealing in apatite, Chemical Geology, v. 198, n. 1-2, p. 107–137, https://doi.org/10.1016/S0009-2541(02)00424-2.

Baughman, J. S., & Flowers, R. M., 2020, Mesoproterozoic burial of the Kaapvaal craton, southern Africa during Rodinia supercontinent assembly from (U-Th)/He thermochronology, Earth and Planetary Science Letters, v. 531, https://doi.org/10.1016/j.epsl.2019.115930.

Beaumont, C., Quinlan, G. M., & Hamilton, J., 1987, The Alleghanian orogeny and its relationship to the evolution of the eastern interior, North America, In C. Beaumont, & A. Tankard (Eds.) Sedimentary Basins and Basin-Forming Mechanisms — Memoir 12, p. 425–445. Canadian Society of Petroleum Geologists, Memoir 12.

Bell, M., & Laine, E. P., 1985, Erosion of the Laurentide region of North America by glacial and glaciofluvial processes, Quaternary Research, v. 23, n. 2, p. 154–174, https://doi.org/10.1016/0033-5894(85)90026-2.

Bond, G., 1978, Speculations on real sea-level changes and vertical motions of continents at selected times in the Cretaceous and Tertiary Periods, Geology, v. 6, n. 4, p. 247–250.

Burgess, P. M., 2019, Phanerozoic Evolution of the Sedimentary Cover of the North American Craton, In The Sedimentary Basins of the United States and Canada, p. 39–75. Elsevier, https://doi.org/10.1016/B978-0-444-63895-3.00002-4.

Burgess, P. M., Gurnis, M., & Moresi, L., 1997, Formation of sequences in the cratonic interior of North America by interaction between mantle, eustatic, and stratigraphic processes, Geological Society of America Bulletin, v. 109, n. 12, p. 1515–1535, https://doi.org/10.1130/0016-7606(1997)109<1515:FOSITC>2.3.CO;2.

Burrus, J., Osadetz, K., Wolf, S., Doligez, B., Visser, K., & Dearborn, D., 1996, A two-dimensional regional basin model of Williston Basin hydrocarbon systems, AAPG Bulletin, v. 80, n. 2, p. 265–291, https://doi.org/10.1306/64ed87aa-1724-11d7-8645000102c1865d.

Butcher, G. S., Kendall, A. C., Boyce, A. J., Millar, I. L., Andrews, J. E., & Dennis, P. F., 2012, Age determination of the Lower Watrous red-beds of the Williston Basin, Saskatchewan, Canada, Bulletin of Canadian Petroleum Geology, v. 60, n. 4, p. 227–238, https://doi.org/10.2113/gscpgbull.60.4.227.

Carlson, W. D., 1990, Mechanisms and kinetics of apatite fission-track annealing, American Mineralogist, v. 75, n. 9-10, p. 1120–1139.

Carlson, W. D., Donelick, R. A., & Ketcham, R. A., 1999, Variability of apatite fission-track annealing kinetics: I. Experimental results, American Mineralogist, v. 84, n. 9, p. 1213–1223, https://doi.org/10.2138/am-1999-0901.

Carpéna, J., Kienast, J.-R., Ouzegane, K., & Jehanno, C., 1988, Evidence of the contrasted fission-track clock behavior of the apatites from In Ouzzal carbonatites (northwest Hoggar): The low-temperature thermal history of an Archean basement, Geological Society of America Bulletin, v. 100, p. 1237–1243.

Catacosinos, P. A., Daniels Jr., P. A., & Harrison III, W. B., 1990, Structure, Stratigraphy, and Petroleum Geology of the Michigan Basin, In M. W. Leighton, D. R. Kolata, D. F. Oltz, & J. J. Eidel (Eds.) Interior Cratonic Basins, v. 51, p. 561–601. American Association of Petroleum Geologists, https://doi.org/10.1306/M51530C31.

Chew, D. M., & Donelick, R. A., 2012, Combined apatite fission track and U-Pb dating by LA-ICP-MS and its application in apatite provenance analysis, In P. Sylvester (Ed.) Quantitative mineralogy and microanalysis of sediments and sedimentary rocks, v. 42, p. 219–248. Mineralogical Association of Canada.

Cogné, N., Chew, D. M., Donelick, R. A., & Ansberque, C., 2020, LA-ICP-MS apatite fission track dating: A practical zeta-based approach, Chemical Geology, v. 531, p. 119302, https://doi.org/10.1016/j.chemgeo.2019.119302.

Cogné, N., & Gallagher, K., 2021, Some comments on the effect of uranium zonation on fission track dating by LA-ICP-MS, Chemical Geology, v. 573, p. 120226, https://doi.org/10.1016/j.chemgeo.2021.120226.

Crowley, K. D., 1985, Thermal significance of fission-track length distributions, Nuclear Tracks and Radiation Measurements (1982), v. 10, n. 3, p. 311–322, https://doi.org/10.1016/0735-245X(85)90120-6.

Crowley, K. D., 1991, Thermal history of Michigan Basin and Southern Canadian Shield from apatite fission track analysis, Journal of Geophysical Research, v. 96, n. B1, p. 697–711, https://doi.org/10.1029/90JB02174.

Crowley, K. D., Cameron, M., & McPherson, B. J., 1990, Annealing of etchable fission-track damage in F-, OH-, Cl- and Sr-apatite. 1. Systematics and preliminary interpretations, Nuclear Tracks and Radiation Measurements, v. 17, n. 3, p. 409–410, https://doi.org/10.1016/1359-0189(90)90066-7.

Crowley, K. D., & Kuhlman, S. L., 1988, Apatite thermochronometry of Western Canadian Shield: Implications for origin of the Williston Basin, Geophysical Research Letters, v. 15, n. 3, p. 221–224, https://doi.org/10.1029/GL015i003p00221.

Crowley, K. D., Naeser, C. W., & Babel, C. A., 1986, Tectonic significance of precambrian apatite fission-track ages from the midcontinent United States, Earth and Planetary Science Letters, v. 79, n. 3-4, p. 329–336, https://doi.org/10.1016/0012-821X(86)90189-5.

DeConto, R. M., Pollard, D., Wilson, P. A., Pälike, H., Lear, C. H., & Pagani, M., 2008, Thresholds for Cenozoic bipolar glaciation, Nature, v. 455, n. 7213, p. 652–656, https://doi.org/10.1038/nature07337.

Donelick, R. A., Ketcham, R. A., & Carlson, W. D., 1999, Variability of apatite fission-track annealing kinetics; II, Crystallographic orientation effects, American Mineralogist, v. 84, n. 9, p. 1224–1234, https://doi.org/10.2138/am-1999-0902.

Donelick, R. A., O'Sullivan, P. B., & Ketcham, R. A., 2005, Apatite Fission-Track Analysis, Reviews in Mineralogy and Geochemistry, v. 58, n. 1, p. 49–94, https://doi.org/10.2138/rmg.2005.58.3.

Duddy, I. R., Green, P. F., & Laslett, G. M., 1988, Thermal annealing of fission tracks in apatite 3. Variable temperature behaviour, Chemical Geology: Isotope Geoscience Section, v. 73, n. 1, p. 25–38, https://doi.org/10.1016/0168-9622(88)90019-X.

Eldrett, J. S., Harding, I. C., Wilson, P. A., Butler, E., & Roberts, A. P., 2007, Continental ice in Greenland during the Eocene and Oligocene, Nature, v. 446, n. 7132, p. 176–179, https://doi.org/10.1038/nature05591.

Feinstein, S., Kohn, B., Osadetz, K., Everitt, R., & O'Sullivan, P., 2009, Variable Phanerozoic thermal history in the Southern Canadian Shield: Evidence from an apatite fission track profile at the Underground Research Laboratory (URL), Manitoba, Tectonophysics, v. 475, n. 1, p. 190–199, https://doi.org/10.1016/j.tecto.2009.01.016.

Fernie, N., Glorie, S., Jessell, M. W., & Collins, A. S., 2018, Thermochronological insights into reactivation of a continental shear zone in response to Equatorial Atlantic rifting (northern Ghana), Scientific Reports, v. 8, n. 1, https://doi.org/10.1038/s41598-018-34769-x.

Fleischer, R. L., Price, P. B., & Walker, R. M., 1965, Effects of temperature, pressure, and ionization of the formation and stability of fission tracks in minerals and glasses, Journal of Geophysical Research, v. 70, n. 6, p. 1497–1502, https://doi.org/10.1029/jz070i006p01497.

Flowers, R., Bowring, S., & Reiners, P., 2006, Low long-term erosion rates and extreme continental stability documented by ancient (U-Th)/He dates, Geology, v. 34, n. 11, p. 925, https://doi.org/10.1130/G22670A.1.

Flowers, R. M., Ault, A. K., Kelley, S. A., Zhang, N., & Zhong, S., 2012, Epeirogeny or eustasy? Paleozoic-Mesozoic vertical motion of the North American continental interior from thermochronometry and implications for mantle dynamics, Earth and Planetary Science Letters, v. 317, p. 436–445, https://doi.org/10.1016/j.epsl.2011.11.015.

Fox, M., & Carter, A., 2020, Heated Topics in Thermochronology and Paths towards Resolution, Geosciences, v. 10, n. 9, p. 375, https://doi.org/10.3390/geosciences10090375.

Fraser, J. A., Donaldson, J. A., Fahrig, W. F., & Tremblay, L. P., 1970, Helikian basins and geosynclines of the northwestern Canadian Shield, In A. J. Baer (Ed.) Symposium on basins and geosynclines of the Canadian Shield, v. 70, p. 213–238. Ottawa, Ontario: Geological Survey of Canada, Paper 70-40.

Galbraith, R. F., 2005, Statistics for fission track analysis, Boca Raton, FL: Chapman and Hall/CRC, Taylor and Francis Group, https://doi.org/10.1198/jasa.2007.s165.

Galbraith, R. F., & Green, P. F., 1990, Estimating the component ages in a finite mixture, International Journal of Radiation Applications and Instrumentation. Part D. Nuclear Tracks and Radiation Measurements, v. 17, n. 3, p. 197–206, https://doi.org/10.1016/1359-0189(90)90035-V.

Gallagher, K., 2012, Transdimensional inverse thermal history modeling for quantitative thermochronology, Journal of Geophysical Research: Solid Earth, v. 117, n. B2, https://doi.org/10.1029/2011JB008825.

Gallagher, K., 2016, Comment on 'A reporting protocol for thermochronologic modeling illustrated with data from the Grand Canyon' by Flowers, Farley and Ketcham.

Gallagher, K., 2021, Comment on "Discussion: Extracting thermal history from low temperature thermochronology/A comment on the recent exchanges between Vermeesch and Tian and Gallagher and Ketcham", by Paul Green and Ian Duddy, Earth Science Reviews, https://doi.org/10.1016/j, Earth-Science Reviews, v. 216, p. 103549, https://doi.org/10.1016/j.earscirev.2021.103549.

Gallagher, K., & Ketcham, R. A., 2018, Comment on "Thermal history modelling: HeFTy vs. QTQt" by Vermeesch and Tian, Earth-Science Reviews (2014), 139, 279–290, Earth-Science Reviews, v. 176, p. 387–394, https://doi.org/10.1016/j.earscirev.2017.11.001.

Gallagher, K., & Ketcham, R. A., 2020, Comment on the reply to the Comment on "Thermal history modelling: HeFTy vs. QTQt" by Vermeesch and Tian, Earth-Science Reviews (2014), 139, 279–290, Earth-Science Reviews, v. 203, p. 102878, https://doi.org/10.1016/j.earscirev.2019.102878.

Galloway, J. M., Armstrong, D., & Lavoie, D., 2012, Palynology of the INCO Winisk #49204 core (54°18'30"N, 87°02'30"W, NTS 43L/6), Ontario, Geological Survey of Canada, Open File 7065, v. , p. 1–51, https://doi.org/10.4095/290985.

Gleadow, A. J., & Duddy, I. R., 1981, A natural long-term track annealing experiment for apatite, Nuclear Tracks, v. 5, n. 1-2, p. 169–174, https://doi.org/10.1016/0191-278X(81)90039-1.

Gleadow, A. J., Duddy, I. R., Green, P. F., & Hegarty, K. A., 1986a, Fission track lengths in the apatite annealing zone and the interpretation of mixed ages, Earth and Planetary Science Letters, v. 78, n. 2-3, p. 245–254, https://doi.org/10.1016/0012-821X(86)90065-8.

Gleadow, A. J., Duddy, I. R., Green, P. F., & Lovering, J. F., 1986b, Confined fission track lengths in apatite: a diagnostic tool for thermal history analysis, Contributions to Mineralogy and Petrology, v. 94, n. 4, p. 405–415, https://doi.org/10.1007/BF00376334.

Glorie, S., Alexandrov, I., Nixon, A., Jepson, G., Gillespie, J., & Jahn, B. M., 2017a, Thermal and exhumation history of Sakhalin Island (Russia) constrained by apatite U-Pb and fission track thermochronology, Journal of Asian Earth Sciences, v. 143, p. 326–342, https://doi.org/10.1016/j.jseaes.2017.05.011.

Glorie, S., Gillespie, J., Jepson, G., & Fernie, N., 2017b, Does Uranium influence fission track annealing in apatite?, In Goldschmidt Abstracts, p. 1366–1366. Paris, France: Geochemical Society.

Gradstein, F. M., Ogg, J. G., Schmitz, M. D., & Ogg, G. M. (Eds.) , 2020, Geologic Time Scale 2020, Elsevier, https://doi.org/10.1016/c2020-1-02369-3.

Green, P., & Duddy, I., 2006, Interpretation of apatite (U–Th)/He ages and fission track ages from cratons, Earth and Planetary Science Letters, v. 244, n. 3-4, p. 541–547, https://doi.org/10.1016/j.epsl.2006.02.024.

Green, P., & Duddy, I., 2021, Discussion: Extracting thermal history from low temperature thermochronology. A comment on recent exchanges between Vermeesch and Tian and Gallagher and Ketcham, Earth-Science Reviews, v. 216, p. 103197, https://doi.org/10.1016/j.earscirev.2020.103197.

Green, P. F., Crowhurst, P. V., Duddy, I. R., Japsen, P., & Holford, S. P., 2006, Conflicting (U-Th)/He and fission track ages in apatite: Enhanced He retention, not anomalous annealing behaviour, Earth and Planetary Science Letters, v. 250, n. 3-4, p. 407–427, https://doi.org/10.1016/j.epsl.2006.08.022.

Green, P. F., & Duddy, I. R., 2012, Thermal History Reconstruction in Sedimentary Basins using Apatite Fission-Track Analysis and Related Techniques, In Analyzing the Thermal History of Sedimentary Basins: Methods and Case Studies, p. 65–104. Society for Sedientary Geology, https://doi.org/10.2110/sepmsp.103.065.

Green, P. F., Duddy, I. R., Gleadow, A. J., Tingate, P. R., & Laslett, G. M., 1985, Fission-track annealing in apatite: Track length measurements and the form of the Arrhenius plot, Nuclear Tracks and Radiation Measurements (1982), v. 10, n. 3, p. 323–328, https://doi.org/10.1016/0735-245X(85)90121-8.

Green, P. F., Duddy, I. R., Gleadow, A. J. W., Tingate, P. R., & Laslett, G. M., 1986, Thermal annealing of fission tracks in apatite, Chemical Geology: Isotope Geoscience section, v. 59, n. C, p. 237–253, https://doi.org/10.1016/0168-9622(86)90074-6.

Green, P. F., Japsen, P., Bonow, J. M., Chalmers, J. A., & Duddy, I. R., 2020, Thermal history solutions from thermochronology must be governed by geological relationships: A comment on Jess et al. (2019), Geomorphology, v. 360, p. 106848, https://doi.org/10.1016/j.geomorph.2019.106848.

Green, P. F., Japsen, P., Bonow, J. M., Chalmers, J. A., Duddy, I. R., & Kukkonen, I. T., 2022, The post-Caledonian thermo-tectonic evolution of Fennoscandia, Gondwana Research, v. 107, p. 201–234, https://doi.org/https://doi.org/10.1016/j.gr.2022.03.007.

Guenthner, W. R., Reiners, P. W., Drake, H., & Tillberg, M., 2017, Zircon, titanite, and apatite (U-Th)/He ages and age-eU correlations from the Fennoscandian Shield, southern Sweden, Tectonics, v. 36, n. 7, p. 1254–1274, https://doi.org/10.1002/2017TC004525.

Guibaldo, C. N., Bordese, S., & Simoy, M. I., 2022, Results report of apatite fission-track analysis by LA-ICP-MS and its comparison with the conventional external detector method of dating, Journal of Analytical Atomic Spectrometry, v. 37, n. 2, p. 369–380, https://doi.org/10.1039/d1ja00284h.

Hendriks, B. W., & Redfield, T. F., 2005, Apatite fission track and (U-Th)/He data from Fennoscandia: An example of underestimation of fission track annealing in apatite, Earth and Planetary Science Letters, v. 236, n. 1-2, p. 443–458, https://doi.org/10.1016/j.epsl.2005.05.027.

Hoffman, P. F., 1988, United plates of America, the birth of a craton: Early Proterozoic assembly and growth of Laurentia, Annual Review of Earth and Planetary Sciences, v. 16, n. 1, p. 543–603, https://doi.org/10.1146/annurev.ea.16.050188.002551.

Hoffman, P. F., 1989, Precambrian geology and tectonic history of North America, In A. W. Bally, & A. R. Palmer (Eds.) The Geology of North America—An Overview, v. A, chap. 16, p. 447–512. Geological Society of America, https://doi.org/10.1130/DNAG-GNA-A.447.

Hyeong, K., Lee, J., Seo, I., Lee, M. J., Yoo, C. M., & Khim, B. K., 2014, Southward shift of the Intertropical Convergence Zone due to Northern Hemisphere cooling at the Oligocene-Miocene boundary, Geology, v. 42, n. 8, p. 667–670, https://doi.org/10.1130/G35664.1.

Issler, D. R., 1996, An inverse model for extracting thermal histories from apatite fission track data: instructions and software for the Windows 95 environment, Tech. rep., Geological Survey of Canada, Open File Report 2325, https://doi.org/10.4095/208313.

Issler, D. R., McDannell, K. T., O'Sullivan, P. B., & Lane, L. S., 2022, Simulating sedimentary burial cycles – Part 2: Elemental-based multikinetic apatite fission-track interpretation and modelling techniques illustrated using examples from northern Yukon, Geochronology, v. 4, n. 1, p. 373–397, https://doi.org/10.5194/gchron-4-373-2022.

Ketcham, R. A., 2005, Forward and Inverse Modeling of Low-Temperature Thermochronometry Data, Reviews in Mineralogy and Geochemistry, v. 58, n. 1, p. 275–314, https://doi.org/10.2138/rmg.2005.58.11.

Ketcham, R. A., 2015, Technical Note: Calculation of stoichiometry from EMP data for apatite and other phases with mixing on monovalent anion sites, American Mineralogist, v. 100, n. 7, p. 1620–1623, https://doi.org/10.2138/am-2015-5171.

Ketcham, R. A., 2019, Fission-Track Annealing: From Geologic Observations to Thermal History Modeling, In M. G. Malusá, & P. G. Fitzgerald (Eds.) Fission-Track Thermochronology and its Application to Geology, chap. 3, p. 49–75. Springer, Cham., https://doi.org/10.1007/978-3-319-89421-8_3.

Ketcham, R. A., Carter, A., Donelick, R. A., Barbarand, J., & Hurford, A. J., 2007, Improved modeling of fission-track annealing in apatite, American Mineralogist, v. 92, n. 5-6, p. 799–810, https://doi.org/10.2138/am.2007.2281.

Ketcham, R. A., Carter, A., & Hurford, A. J., 2015, Inter-laboratory comparison of fission track confined length and etch figure measurements in apatite, American Mineralogist, v. 100, n. 7, p. 1452–1468, https://doi.org/10.2138/am-2015-5167.

Ketcham, R. A., Donelick, R. A., Balestrieri, M. L., & Zattin, M., 2009, Reproducibility of apatite fission-track length data and thermal history reconstruction, Earth and Planetary Science Letters, v. 284, n. 3-4, p. 504–515, https://doi.org/10.1016/j.epsl.2009.05.015.

Ketcham, R. A., Donelick, R. A., & Carlson, W. D., 1999, Variability of apatite fission-track annealing kinetics: III. Extrapolation to geological time scales, American Mineralogist, v. 84, n. 9, p. 1235–1255, https://doi.org/10.2138/am-1999-0903.

Ketcham, R. A., van der Beek, P., Barbarand, J., Bernet, M., & Gautheron, C., 2018, Reproducibility of Thermal History Reconstruction From Apatite Fission-Track and (U-Th)/He Data, Geochemistry, Geophysics, Geosystems, v. 19, n. 8, p. 2411–2436, https://doi.org/10.1029/2018GC007555.

Kohn, B., & Gleadow, A., 2019, Application of Low-Temperature Thermochronology to Craton Evolution, In M. G. Malusá, & P. G. Fitzgerald (Eds.) Fission-Track Thermochronology and its Application to Geology, chap. 21, p. 373–393. Springer, Cham., https://doi.org/10.1007/978-3-319-89421-8_21.

Kohn, B. P., Gleadow, A. J., Brown, R. W., Gallagher, K., O'Sullivan, P. B., & Foster, D. A., 2002, Shaping the Australian crust over the last 300 million years: Insights from fission track thermotectonic imaging and denudation studies of key terranes, Australian Journal of Earth Sciences, v. 49, n. 4, p. 697–717, https://doi.org/10.1046/j.1440-0952.2002.00942.x.

Kohn, B. P., Gleadow, A. J. W., Brown, R. W., Gallagher, K., Lorencak, M., & Noble, W. P., 2005, Visualizing thermotectonic and denudation histories using apatite fission track thermochronology, In P. W. Reiners, & T. A. Ehlers (Eds.) Reviews in

Mineralogy and Geochemistry, v. 58, p. 527–565. Mineralogical Society of America and Geochemical Society, Washington, DC, United States (USA), https://doi.org/10.2138/rmg.2005.58.20.

Kohn, B. P., Lorencak, M., Gleadow, A. J. W., Kohlmann, F., Raza, A., Osadetz, K. G., & Sorjonen-Ward, P., 2009, A reappraisal of low-temperature thermochronology of the eastern Fennoscandia Shield and radiation-enhanced apatite fission-track annealing, Geological Society, London, Special Publications, v. 324, n. 1, p. 193–216.

Kohn, B. P., Osadetz, K. G., & Bezys, R. K., 1995, Apatite fission-track dating of two crater structures in the Canadian Williston Basin, Bulletin of Canadian Petroleum Geology, v. 43, n. 1, p. 54–64.

Kong, J. M., Boucher, D. R., & Smith, B. H. S., 1999, Exploration and geology of the Attawapiskat kimberlites, James Bay lowland, northern Ontario, Canada, In J. J. Gurney, J. L. Gurney, M. D. Pascoe, & S. H. Richardson (Eds.) 7th International Kimberlite Conference, p. 452–467. Cape Town, South Africa.

Laslett, G. M., Green, P. F., Duddy, I. R., & Gleadow, A. J., 1987, Thermal annealing of fission tracks in apatite 2. A quantitative analysis, Chemical Geology: Isotope Geoscience Section, v. 65, n. 1, p. 1–13, https://doi.org/10.1016/0168-9622(87)90057-1.

Laslett, G. M., Kendall, W. S., Gleadow, A. J., & Duddy, I. R., 1982, Bias in measurement of fission-track length distributions, Nuclear Tracks and Radiation Measurements (1982), v. 6, n. 2-3, p. 79–85, https://doi.org/10.1016/0735-245X(82)90031-X.

Lavoie, D., Pinet, N., Dietrich, J., & Chen, Z., 2015, The Paleozoic Hudson Bay Basin in northern Canada: New insights into hydrocarbon potential of a frontier intracratonic Basin, AAPG Bulletin, v. 99, n. 5, p. 859–888, https://doi.org/10.1306/12161414060.

Lavoie, D., Pinet, N., Dietrich, J., Zhang, S., Hu, K., Asselin, E., Chen, Z., Bertrand, R., Galloway, J., Decker, V., Budkewitsch, P., Armstrong, D., Nicolas, M., Reyes, J., Kohn, B. P., Duchesne, M., J, Brake, V., Keating, P., Craven, J., & Roberts, B., 2013, Geological framework, basin evolution, hydrocarbon system data and conceptual hydrocarbon plays for the Hudson Bay and Foxe basins, Canadian Arctic, Tech. rep., Geological Survey of Canada, https://doi.org/10.4095/293119.

Lavoie, D., Pinet, N., Zhang, S., Reyes, J., Jiang, C., Ardakani, O. H., Savard, M. M., Dhillon, R. S., Chen, Z., Dietrich, J., R, Hu, K., Craven, J. A., Roberts, B., Duchesne, M. J., Brake, V. I., Huot-Vézina, G., Galloway, J. M., McCracken, A., D, Asselin, E., Decker, V., Beauchemin, M., Nicolas, M. P. B., Armstrong, D. K., & Hahn, K. E., 2019, Hudson Bay, Hudson Strait, Moose River, and Foxe basins: synthesis of the research activities under the Geomapping for Energy and Minerals (GEM) programs 2008-2018, Tech. rep., Geological Survey of Canada, Open File 8507, https://doi.org/10.4095/314653.

LeFever, R. D., 1996, Sedimentology and Stratigraphy of the Deadwood-Winnipeg Interval (Cambro-Ordovician), Williston Basin, In M. Longman, & M. Sonnenfeld (Eds.) Paleozoic Systems of the Rocky Mountain Region, p. 11–28. Rocky Mountain Section, Society for Sedimentary Geology.

Li, W., Cheng, Y., Feng, L., Niu, J., Liu, Y., Skuratov, V. A., Zdorovets, M. V., Boatner, L. A., & Ewing, R. C., 2021, Alpha-decay induced shortening of fission tracks simulated by in situ ion irradiation, Geochimica et Cosmochimica Acta, v. 299, p. 1–14, https://doi.org/10.1016/j.gca.2021.01.022.

Licciardi, J. M., Clark, P. U., Jenson, J. W., & Macayeal, D. R., 1998, Deglaciation of a soft-bedded Laurentide Ice Sheet, Quaternary Science Reviews, v. 17, n. 4-5, p. 427–448, https://doi.org/10.1016/S0277-3791(97)00044-9.

Lorencak, M., Kohn, B., Osadetz, K., & Gleadow, A., 2004, Combined apatite fission track and (U–Th)/He thermochronometry in a slowly cooled terrane: results from a 3440-m-deep drill hole in the southern Canadian Shield, Earth and Planetary Science Letters, v. 227, n. 1-2, p. 87–104, https://doi.org/10.1016/j.epsl.2004.08.015.

McDannell, K. T., 2020, Notes on statistical age dispersion in fission-track datasets: the chi-square test, annealing variability, and analytical considerations, EarthArXiv, v. , p. 1–4, https://doi.org/10.31223/OSF.IO/UJ4HX.

McDannell, K. T., Brenhin Keller, C., Guenthner, W. R., Zeitler, P. K., & Shuster, D. L., 2022a, Thermochronologic constraints on the origin of the Great Unconformity, Proceedings of the National Academy of Sciences of the United States of America, v. 119, n. 5, p. e2118682119, https://doi.org/10.1073/pnas.2118682119.

McDannell, K. T., & Flowers, R. M., 2020, Vestiges of the Ancient: Deep-Time Noble Gas Thermochronology, Elements, v. 16, n. 5, p. 325–330, https://doi.org/10.2138/gselements.16.5.325.

McDannell, K. T., & Issler, D. R., 2021, Simulating sedimentary burial cycles – Part 1: Investigating the role of apatite fission track annealing kinetics using synthetic data, Geochronology, v. 3, n. 1, p. 321–335, https://doi.org/10.5194/gchron-3-321-2021.

McDannell, K. T., Issler, D. R., & O'Sullivan, P. B., 2019a, Radiation-enhanced fission track annealing revisited and consequences for apatite thermochronometry, Geochimica et Cosmochimica Acta, v. 252, p. 213–239, https://doi.org/10.1016/j.gca.2019.03.006.

McDannell, K. T., & Keller, C. B., 2022, Cryogenian glacial erosion of the central Canadian Shield: The "late" Great Unconformity on thin ice, Geology, v. 50, https://doi.org/10.1130/G50315.1.

McDannell, K. T., Keller, C. B., Guenthner, W. R., Zeitler, P. K., & Shuster, D. L., 2022b, Reply to Flowers et al.: Existing thermochronologic data constrain Snowball glacial erosion below the Great Unconformity, Proceedings of the National Academy of Sciences, v. 119, n. 38, p. e2209946119, https://doi.org/10.1073/pnas.2209946119.

McDannell, K. T., Pinet, N., & Issler, D. R., 2020, Exhuming the Canadian Shield: preliminary interpretations from low-temperature thermochronology and significance for the sedimentary succession of the Hudson Bay Basin, In D. Lavoie, & K. Dewing (Eds.) Sedimentary Basins of the Canadian north — Contributions to a 1000 Ma Geological Journey and Insight on Resource Potential, chap. 10. Geological Survey of Canada, Bulletin 609, https://doi.org/10.31223/X54P5F.

McDannell, K. T., Schneider, D. A., Zeitler, P. K., O'Sullivan, P. B., & Issler, D. R., 2019b, Reconstructing deep-time histories from integrated thermochronology: An example from southern Baffin Island, Canada, Terra Nova, v. 31, n. 3, p. 189–204, https://doi.org/10.1111/ter.12386.

Metsaranta, R. T., & Houlé, M. G., 2017, Precambrian geology, McFaulds Lake area, "Ring of Fire" region, Ontario, central sheet, Geological Survey of Canada, Open File 8201, scale 1:100,000, v. P.3805, https://doi.org/10.4095/299711.

Mills, B. J., Krause, A. J., Scotese, C. R., Hill, D. J., Shields, G. A., & Lenton, T. M., 2019, Modelling the long-term carbon cycle, atmospheric CO2, and Earth surface temperature from late Neoproterozoic to present day.

Morón, S., Kohn, B. P., Beucher, R., Mackintosh, V., Cawood, P. A., Moresi, L., & Gallagher, S. J., 2020, Denuding a Craton: Thermochronology Record of Phanerozoic Unroofing From the Pilbara Craton, Australia, Tectonics, v. 39, n. 9, p. e2019TC005988, https://doi.org/10.1029/2019TC005988.

Murray, K. E., Stevens Goddard, A. L., Abbey, A. L., & Wildman, M., 2022, Thermal history modeling techniques and interpretation strategies: Applications using HeFTy, Geosphere, v. , https://doi.org/10.1130/GES02500.1.

Naeser, C. W., & Crowley, K. D., 1990, Fission-track dating of apatite from deep borehole ATK-1 at Atikokan, Ontario, In Z. E. Peterman, & D. C. Kamineni (Eds.) Isotopic studies of the Eye-Dashwa Lakes Pluton and the long-term integrity of whole-rock and mineral systems, p. 57–64. Pinawa, Manitoba: Atomic Energy of Canada Limited.

Nelson, S. J., 1963, Ordovician paleontology of the northern Hudson Bay lowland, Memoir of the Geological Society of America, v. 90, n. 1, p. 1–145, https://doi.org/10.1130/MEM90-p1.

Norris, A., 1993, Hudson Platform – Geology, In D. Stott, & J. Aitken (Eds.) Sedimentary Cover of the Craton in Canada, p. 653–700. The Geological Society of America, https://doi.org/10.1130/dnag-gna-d1.653.

Norris, A. W., & Sanford, B. V., 1968, Paleozoic and Mesozoic Geology of the Hudson Bay Lowlands, Tech. rep., Geological Survey of Canada, Paper no. 68-53, Ottawa, Ontario, https://doi.org/10.4095/119794.

Norris, G., 1977, Palynofloral evidence for terrestrial Middle Jurassic in the Moose River Basin, Ontario, Canadian Journal of Earth Sciences, v. 14, n. 2, p. 153–158, https://doi.org/10.1139/e77-018.

Osadetz, K., Kohn, B., Feinstein, S., & O'Sullivan, P., 2002, Thermal history of Canadian Williston basin from apatite fission-track thermochronology—implications for petroleum systems and geodynamic history, Tectonophysics, v. 349, n. 1-4, p. 221–249, https://doi.org/10.1016/S0040-1951(02)00055-0.

O'Sullivan, P., 2018, Statistical evaluation (and manipulation) of fission-track single-grain age data: an analyst's "unbiased" perspective, In 16th International Conference on Thermochronology, p. 1. Palais Salfeldt, Quedlinburg, Germany: Thermo2018.

Patchett, P. J., Ross, G. M., & Gleason, J. D., 1999, Continental drainage in North America during the phanerozoic from Nd isotopes, Science, v. 283, n. 5402, p. 671–673, https://doi.org/10.1126/science.283.5402.671.

Percival, J. A., Skulski, T., Sanborn-Barrie, M., Stott, G. M., Leclair, A. D., Corkery, M. T., & Boily, M., 2012, Geology and Tectonic Evolution of the Superior Province, Canada, In J. A. Percival, F. A. Cook, & R. M. Clowes (Eds.) Tectonic Styles in Canada: The LITHOPROBE Perspective, v. 49, p. 321–378. Geological Association of Canada, Special Paper.

Peters, S. E., Husson, J. M., & Czaplewski, J., 2018, Macrostrat: A platform for geological data integration and deep-time earth crust research, Geochemistry, Geophysics, Geosystems, v. 19, n. 4, p. 1393–1409, https://doi.org/10.1029/2018GC007467.

Pinet, N., Kohn, B., Lavoie, D., & Canada, N. R., 2016, The ups and downs of the Canadian Shield: 1- preliminary results of apatite fission track analysis from Hudson Bay region, Open File Report 8110, v. , p. 1–59, https://doi.org/https://doi.org/10.4095/299248.

Pinet, N., Lavoie, D., Dietrich, J., Hu, K., & Keating, P., 2013, Architecture and subsidence history of the intracratonic Hudson Bay Basin, northern Canada, Earth-Science Reviews, v. 125, p. 1–23, https://doi.org/10.1016/j.earscirev.2013.05.010.

Pinet, N., & McDannell, K. T., 2020, The ups and downs of the Canadian Shield : 3 – additional apatite fission-track analyses from the Musselwhite, Roberto, Meadowbank and Raglan mines, Ontario, Quebec, and Nunavut, Geological Survey of Canada, Open File Report 8706, v. , p. 1–51, https://doi.org/10.4095/321845.

Price, W. L., 1977, A controlled random search procedure for global optimisation, The Computer Journal, v. 20, n. 4, p. 367–370, https://doi.org/10.1093/comjnl/20.4.367.

Rahn, M., & Seward, D., 2000, How many track lengths do we need?, On Track (unpublished newsletter), v. 10, p. 14–17.

Rainbird, R. H., Stern, R. A., Rayner, N., & Jefferson, C. W., 2007, Age, provenance, and regional correlation of the Athabasca Group, Saskatchewan and Alberta, constrained by igneous and detrital zircon geochronology, Tech. rep., Geological Survey of Canada, https://doi.org/10.4095/223761.

Ravenhurst, C. E., Roden-Tice, M. K., & Miller, D. S., 2003, Thermal annealing of fission tracks in fluorapatite, chlorapatite, manganoanapatite, and Durango apatite: Experimental results, Canadian Journal of Earth Sciences, v. 40, n. 7, p. 995–1007, https://doi.org/10.1139/e03-032.

Rayner, N., 2010, Far North Geomapping Initiative: new U-Pb geochronological results from the Seal River region, northeastern Manitoba (parts of NTS 54L, M, 64I, P), In Report of Activities 2010, p. 23–35. Manitoba Innovation, Energy and Mines, Manitoba Geological Survey.

Sage, R. P., 2000, Kimberlites of the Attawapiskat area, James Bay Lowlands, northern Ontario, Ontario Geological Survey, Open File Report, v. 6019, p. 1–341.

Sanford, B., 1987, Paleozoic Geology of the Hudson Platform, In C. Beaumont, & A. Tankard (Eds.) Sedimentary Basins and Basin-Forming Mechanisms, v. Memoir 12, p. 483–505. Canadian Society of Petroleum Geologists.

Sanford, B. V., & Grant, A. C., 1990, New findings relating to the stratigraphy and structure of the Hudson Platform, In Current Research Part D, Interior Plains and Arctic Canada, v. 90-1D, p. 17–30. Geological Survey of Canada, https://doi.org/10.4095/131335.

Sanford, B. V., & Norris, A. W., 1973, The Hudson Platform, Canadian Society of Petroleum Geology Special Publications, v. Future Pet, p. 387–409.

Sanford, B. V., Thompson, F. J., & McFall, G. H., 1985, Plate tectonics-a possible controlling mechanism in the development of hydrocarbon traps in southwestern Ontario., Bulletin of Canadian Petroleum Geology, v. 33, n. 1, p. 52–71, https://doi.org/10.35767/gscpgbull.33.1.052.

Schneider, D. A., Heizler, M. T., Bickford, M. E., Wortman, G. L., Condie, K. C., & Perilli, S., 2007, Timing constraints of orogeny to cratonization: Thermochronology of the Paleoproterozoic Trans-Hudson orogen, Manitoba and Saskatchewan, Canada, Precambrian Research, v. 153, p. 65–95.

Scotese, C. R., Song, H., Mills, B. J., & van der Meer, D. G., 2021, Phanerozoic paleotemperatures: The earth's changing climate during the last 540 million years, Earth-Science Reviews, v. 215, p. 103503, https://doi.org/10.1016/j.earscirev.2021.103503.

Seiler, C., Gleadow, A. J. W., & Kohn, B. P., 2013, Apatite fission track dating by LA-ICP-MS and External Detector Method: How do they stack up?, In American Geophysical Union, Fall Meeting 2013, p. T42C–07.

Sloss, L. L., 1963, Sequences in the cratonic interior of north America, Bulletin of the Geological Society of America, v. 74, n. 2, p. 93–114, https://doi.org/10.1130/0016-7606(1963)74[93:SITCIO]2.0.CO;2.

Sugden, D. E., 1978, Glacial Erosion by the Laurentide Ice Sheet, Journal of Glaciology, v. 20, n. 83, p. 367–391, https://doi.org/10.3189/s0022143000013915.

Telford, P. G., & Long, D. G., 1986, Mesozoic Geology of the Hudson Platform, In Elsevier Oceanography Series, v. 44, chap. 3, p. 43–54. Elsevier, https://doi.org/10.1016/S0422-9894(08)70896-1.

Tello, C. A., Palissari, R., Hadler, J. C., Iunes, P. J., Guedes, S., Curvo, E. A., & Paulo, S. R., 2006, Annealing experiments on induced fission tracks in apatite: Measurements of horizontal-confined track lengths and track densities in basal sections and randomly oriented grains, American Mineralogist, v. 91, n. 2-3, p. 252–260, https://doi.org/10.2138/am.2006.1269.

Tillement, B. A., Peniguel, G., & Guillemin, J. P., 1976, Marine Pennsylvanian Rocks in Hudson Bay, Bulletin of Canadian Petroleum Geology, v. 24, n. 3, p. 418–439, https://doi.org/10.35767/gscpgbull.24.3.418.

Trettin, H., 1975, Investigations of Lower Paleozoic geology, Foxe Basin, northeastern Melville Peninsula, and parts of northwestern and central Baffin Island, Geological Survey of Canada Bulletin, v. 251, p. 1–171.

Tripati, A., & Darby, D., 2018, Evidence for ephemeral middle Eocene to early Oligocene Greenland glacial ice and pan-Arctic sea ice, Nature Communications, v. 9, p. 1038, https://doi.org/10.1038/s41467-018-03180-5.

Tukey, J. W., 1962, The Future of Data Analysis, The Annals of Mathematical Statistics, v. 33, n. 1, p. 1–67.

Vermeesch, P., 2009, RadialPlotter: A Java application for fission track, luminescence and other radial plots, Radiation Measurements, v. 44, n. 4, p. 409–410, https://doi.org/10.1016/j.radmeas.2009.05.003.

Vermeesch, P., 2017, Statistics for LA-ICP-MS based fission track dating, Chemical Geology, v. 456, p. 19–27, https://doi.org/10.1016/j.chemgeo.2017.03.002.

Vermeesch, P., 2018, IsoplotR: A free and open toolbox for geochronology, Geoscience Frontiers, v. 9, n. 5, p. 1479–1493, https://doi.org/10.1016/j.gsf.2018.04.001.

Vermeesch, P., 2019, Statistics for Fission-Track Thermochronology, In M. G. Malusa, & P. Fitzgerald (Eds.) Fission-Track Thermochronology and its Application to Geology, chap. 6, p. 109–122. New York: Springer International Publishing, 1 ed., https://doi.org/10.1007/978-3-319-89421-8_6.

Vermeesch, P., & Tian, Y., 2014, Thermal history modelling: HeFTy vs. QTQt, Earth-Science Reviews, v. 139, p. 279–290, https://doi.org/10.1016/j.earscirev.2014.09.010.

Webb, K. J., Scott Smith, B. H., Paul, J. L., & Hetman, C. M., 2004, Geology of the Victor Kimberlite, Attawapiskat, Northern Ontario, Canada: cross-cutting and nested craters, Lithos, v. 76, n. 1-4, p. 29–50, https://doi.org/10.1016/j.lithos.2004.03.050.

Weller, O. M., & St-Onge, M. R., 2017, Record of modern-style plate tectonics in the Palaeoproterozoic Trans-Hudson orogen, Nature Geoscience, v. 10, n. 4, p. 305–311, https://doi.org/10.1038/ngeo2904.

Wheeler, J. O., Hoffman, P., Card, K. D., Davidson, A., Sanford, B. V., Okulitch, A. V., & Roest, W. R., 1996, Geological map of Canada, "A" Series Map 1860A, v. 3 sheets, p. scale 1:5,000,000, https://doi.org/10.4095/208175.

White, T. S., Witzke, B. J., & Ludvigson, G. A., 2000, Evidence for an Albian Hudson arm connection between the Cretaceous Western Interior Seaway of North America and the Labrador Sea, Geological Society of America Bulletin, v. 112, n. 9, p. 1342–1355, https://doi.org/10.1130/0016-7606(2000)112<1342:EFAAHA>2.0.CO;2.

White, W. A., 1973, Deep Erosion by Infracambrian Ice Sheets, Geological Society of America Bulletin, v. 84, n. 5, p. 1841, https://doi.org/10.1130/0016-7606(1973)84<1841:DEBIIS>2.0.CO;2.

Willett, S. D., 1997, Inverse modeling of annealing of fission tracks in apatite 1: A controlled random search method, American Journal of Science, v. 297, n. 10, p. 939–969, https://doi.org/10.2475/ajs.297.10.939.

Williams, G., & Barrs, M., 1976, Palynological analysis of the interval 1130–1260 feet from Aquitaine et al., Narwhal O-58, Hudson Bay, Paleontological Report EPGS-PAL, v. 11-77GLW, p. 1–4.

Zhang, S., & Riva, J. F., 2018, The stratigraphic position and the age of the Ordovician organic-rich intervals in the northern Hudson Bay, Hudson Strait, and Foxe basins—evidence from graptolites, Canadian Journal of Earth Sciences, v. 55, n. 8, p. 897–904, https://doi.org/10.1139/cjes-2017-0266.